Emittance Calculations and Measurements for a Sputter-Type Negative Ion Source

J.H. Billen

September 1983

UWFDM-560

Submitted to Nuclear Instruments and Methods.

FUSION TECHNOLOGY INSTITUTE

UNIVERSITY OF WISCONSIN

MADISON WISCONSIN

Emittance Calculations and Measurements for a Sputter-Type Negative Ion Source

J.H. Billen

Fusion Technology Institute
University of Wisconsin
1500 Engineering Drive
Madison, WI 53706

http://fti.neep.wisc.edu

September 1983

UWFDM-560

Submitted to Nuclear Instruments and Methods.

EMITTANCE CALCULATIONS AND MEASUREMENTS FOR A SPUTTER-TYPE NEGATIVE ION SOURCE

James H. Billen

Fusion Engineering Program
Nuclear Engineering Department
University of Wisconsin-Madison
Madison, Wisconsin 53706

September 1983

UWFDM-560

Submitted to Nuclear Instruments and Methods.

EMITTANCE CALCULATIONS AND MEASUREMENTS FOR A SPUTTER-TYPE NEGATIVE-ION SOURCE†

JAMES H. BILLEN

University of Wisconsin, Madison, Wisconsin 53706, U.S.A.

ABSTRACT

A method for calculating the beam current and emittance of a negative-ion beam from a sputter-type source is described. In this ion source a Cs^+ beam of up to several mA originates by surface ionization on a hot, high-work-function surface. Cs^+ ions with an energy of a few keV strike the Cs-coated cathode where they produce by sputtering negative ions of the cathode material. The calculation involves tracing trajectories of the Cs^+ ions that bombard the cathode surface and also trajectories of the sputtered negative ions. The dependence of the beam current, emittance and average brightness on several ion source parameters is discussed. These parameters include the cathode voltage and details of the ion source geometry such as cathode shape and exit-aperture diameter. Results of the calculations are in good agreement with measurements of emittance for cases in which space charge effects are negligible. For negative-ion currents greater than a few tens of μA and for Cs^+ currents greater than 1-2 mA the measured emittance generally exceeds the calculated emittance if space charge is neglected in the calculation.

ABSTRACT (cont'd)

The calculations have suggested several improvements in the design of the source that were later implemented experimentally to optimize utilization of the Cs^+ beam and to increase the negative-ion extraction efficiency. The ion source lifetime, beam energy spread and the effects of cathode erosion are also discussed.

---

† Work supported in part by the U.S. Department of Energy and the National Science Foundation.

1. Introduction

A good negative-ion beam for use with a tandem electrostatic accelerator is characterized by high intensity and low emittance. The emittance of an ion beam describes the beam quality and tells what fraction is useable in a given application. Emittance is the volume occupied by the particles of the beam in a six-dimensional phase space of position and momentum coordinates. For noninteracting particles subject to conservative forces Liouville's theorem [1]) declares that the magnitude of emittance (though not its shape) is a constant of the motion. Furthermore, if the motions associated with the three spatial dimensions are independent, then the area occupied by the beam in each two-dimensional phase plane of a spatial coordinate and its corresponding momentum coordinate is separately conserved. Thus the emittance at the moment of beam formation is an invariant property of the beam that a well-designed beam transport system will preserve as the beam propagates from the ion source through other components of the system to a target. Various physical effects involving nonconservative forces in beam transport components may degrade (i.e. increase) the beam emittance, but the emittance cannot be improved without extraordinary means generally not available in electrostatic accelerator systems.

A few years ago a new and very successful sputter-type negative-ion source was developed by Richards and students at Wisconsin[2,3]) and independently by Middleton at Pennsylvania[4]). With appropriate cathode materials these sources produce intense, low-emittance beams of elements throughout the periodic table. The earliest source of this type was probably the one reported by Ayukhanov and Chernenko[5]). At Wisconsin

the ion source SNICS (for Source of Negative Ions by Cesium Sputtering) shown in fig. 1 is used chiefly by the fusion engineering group to study radiation damage in potential first-wall materials for fusion reactors. These radiation damage studies require beams of various metal ions preferably of the same material being irradiated to avoid possible problems with contaminant precipitates in the irradiated specimens. For such "self-ion" irradiations SNICS has provided beams of Al_2^-, Cu^- and Ni^-, while on the test bench it has also produced useable beams of H^-, Li^-, B^-, C^-, O^-, TiH^-, V^-, Fe^-, and Ta^-. Beams of $^7Li^-$, $^{12}C^-$, and $^{13}C^-$ have been used for nuclear physics experiments. A commercial version of the source manufactured by National Electrostatics Corporation (NEC) produces intense B^- and B_2^- beams for the injector of a tandem-accelerator-based ion-implantation system[6]). Another NEC SNICS will provide a variety of heavy-ion beams for nuclear physics research. There is also interest in beams of P^-, As^-, and Ga^- for ion implantation, and in negative-ion beams of refractory metals such as titanium and molybdenum for radiation damage studies.

In SNICS 1- to 8-keV Cs^+ ions sputter the cathode's cesium-coated solid surface. Sputtered negative ions of the cathode material accelerate across the cathode-to-anode potential difference and emerge from a 3-mm diameter exit aperture. The Cs^+ beam of up to several mA originates by surface ionization on a hot tungsten helix that is coaxial with the sputter cathode and exit aperture. A treatment of this source as a surface ionization gauge leads to an estimate for the Cs vapor pressure between 10^{-4} and 10^{-5} Torr, and hence Cs^+-ion mean free paths that are 5 to 50 times larger than the (~ 30 mm) dimensions of the source. Thus most Cs^+ ions produced on the ionizer surface strike the cathode after following trajectories dictated by the electric field and without undergoing col-

lisions. The weak magnetic field produced by current flowing in the ionizer helix has a negligible effect on the massive Cs^+ ions, but it may serve to trap electrons and thereby neutralize some Cs^+ space charge. These considerations suggest a very simple model in which electrostatic forces on the Cs^+ ions and on the sputtered negative ions dominate the behavior of the ion source. It should be possible, in principle, to calculate the electrostatic potential in which the ions move, solve for the trajectories of the negative ions, and hence determine the two-dimensional phase space distribution of the ions that emerge from the exit aperture of the ion source. The emittance so derived may be compared directly with measurements of emittance for the source configuration and operating parameters used in the calculation.

1.1 Notation

To facilitate reading the sections that follow, table 1 defines various coordinate systems and symbols used throughout the paper. The beam direction and symmetry axis is along z in either rectangular coordinates (x,y,z) or cylindrical coordinates (r,θ,z). Primes (as in x') refer to differentiation with respect to z and denote phase space divergence coordinates or slopes of trajectories. Dots over position coordinate symbols denote velocities or differentiation with respect to time. The x direction corresponds to $\theta = 0$. We reserve the symbol θ for the azimuthal angle of the cylindrical coordinate system. Angles of incidence are denoted by the symbol α and angles of emission from a surface are denoted by ϕ. Both α and ϕ measure angles with respect to the surface normal direction. The symbol L refers to angular momentum about $r = 0$ and the symbols E_r and E_z denote electric field components along coordinates r and z respectively. Definitions for a few other symbols appear in the text as needed.

2. Negative-ion beam formation

Negative-ion beam formation in the sputter source may be summarized as follows: Cesium positive ions emerge from the ionizer with some initial low energy and follow trajectories determined by the electric field. Most of these now-energetic Cs^+ ions strike the face of the sputter cathode and sputter neutral atoms and ions of the cathode material. These sputtered particles leave the surface with a distribution in both energy and angle. The sputtered negative ions then gain energy rapidly and follow trajectories determined by the electric field. They finally either emerge from the exit aperture of the ion source or they strike some electrode at anode potential. Negative ions that emerge from the exit aperture are characterized by their position and divergence coordinates in the ion beam's phase space distribution.

Our approach to constructing the beam's space brightness distribution is to trace a large number of sputtered negative-ion trajectories distributed over the entire parameter space affecting the ion current associated with each individual trajectory. The physics of the sputtering process dictates what parameters will be important in determining the negative-ion sputtering yield for Cs^+ ions incident on the cathode materials. Important parameters include the energy and angle of incidence of the Cs^+ ions, the angular distribution of the sputtered ions, the energy spectrum of the sputtered ions and properties of the target material. The chief objective of this work is to predict the performance of the sputter source for various choices of electrode configuration and potential. While one would prefer published experimental data for each fundamental process that affects the sputtering yield, such data are generally unavailable except for

a few specific combinations of target material and incident Cs^+ energy. A number of authors[7-11]) have presented thorough reviews of experimental sputtering measurements. Theoretical treatments[12-14]) of the sputtering process coupled with the available data can provide realistic choices for the functional form of the relevant physical processes. The following sections briefly discuss each of these factors.

The sputtering rate of the cathode surface as a function of the radial position determines the negative-ion current associated with each trajectory that we trace. We assume the cathode is a cylinder of revolution with an arbitrarily shaped end facing the ionizer and exit aperture and we calculate this radial dependence of the sputtering rate by tracing a large number of Cs^+-ion trajectories whose initial coordinates are distributed evenly over all of the available surface area of the hot tungsten ionizer. Each Cs^+ trajectory represents a portion of the total ion current incident on the cathode.

2.1 Cs^+-ion initial energy and angular distribution

The Cs^+ ions form by surface ionization on a hot tungsten surface. A theoretical treatment of this phenomenon[8]) assumes that the adsorbed atoms come to thermal equilibrium with the surface and then evaporate as either positive ions or neutral atoms depending upon the difference between the surface work function and the ionization potential of the atom. Hence the energy of the evaporated ions is of the order of kT where k is the Boltzmann constant and T is the temperature of the surface. Even for a very hot surface (~ 1500°C) these initial energies are small compared with the typical potential difference between the ionizer and sputter cathode and have little influence on the shape of the Cs^+ trajectory. We assumed an initial energy of 0.15 eV and a cos ϕ angular distribution

for the Cs^+ ions. For comparison we did a calculation in which all the Cs^+ ions emerged normal to the surface. The low initial energy of the Cs^+ ions should make the angular distribution unimportant. For similar numbers of trajectories in the two cases the differences in the distribution of Cs^+ current on the sputter cathode were no larger than those expected from statistical sampling fluctuations. We continued to use the cosine distribution because there was no saving in the cost of the calculation by ignoring this effect.

2.2 Sputtering yield considerations

We also need negative-ion sputtering yields for Cs^+ ions incident on cesiated metal surfaces. Subsequent to Krohn's[15]) first observation of enhancement in the yield of negative ions sputtered from a surface coated by a layer of alkali atoms, there have been a number of attempts[16-18]) to understand the physics of the process. Direct quantitative yield measurements are scarce for sputtered negative ions. Following previous practice[19-21]) we assumed that the negative-ion yield S^- is proportional to the total sputter yield:

$$S^- = f^- S \tag{1}$$

where f^- is the negative ion fraction. We further assume that f^- is independent of the energy and angle of incidence of the Cs^+ ions and also independent of the energy and the angular distribution of the sputtered particles themselves. Presumably f^- depends upon the electron affinity of the sputtered material, the surface work function (which in turn depends upon the degree of cesium coverage) and perhaps upon other parameters. For this calculation, however, we treat f^- as a constant and choose a plausible value of 2%. The beam intensity that the calculation predicts

scales as f^-. With fixed f^-, the negative-ion sputtering yield has the same dependence as the total sputtering yield S as indicated by eq. (1).

2.2.1 Sputtering yield vs. angle of incidence

There appears to be no a priori reason to expect the same dependence of the sputtering yield on the angle of incidence for either different cathode materials or for different incident energies. Indeed the reviews of this subject by Andersen and Bay[11]) and by Kaminsky[9]) indicate that the situation is quite complicated if one considers a wide range of incident energies or incident-ion masses. Fortunately we are concerned here with only a single incident-ion species, namely Cs^+, over a fairly narrow energy range. Sigmund[12]) has calculated the sputtering yield predicted by the theory of atomic collision cascades. For backward sputtering by ion beams in the few-keV energy range, the collisions are elastic and the sputtering yield is the product of a term which is essentially the stopping power for the ion and a monotonically increasing function of the angle of incidence. For target-to-ion mass ratios m_2/m_1 less than 3 and for angles of incidence less oblique than $\alpha \sim 70°$ the angular dependence is insensitive to both the ion energy and the mass ratio and is approximately $(\cos \alpha)^{-5/3}$, in good agreement with experimental data[12]). The condition on the mass ratio ($m_2/m_1 \leq 3$) is satisfied for Cs^+ ions incident on any cathode material. Figure 2 shows the form of the sputter rate as a function of angle of incidence that we assumed for this calculation. Most Cs^+ trajectories strike the cathode at angles much less oblique than 70°. We divide the sputtering surface into 50 annular zones and count the number of Cs^+ trajectories that strike each zone with each trajectory weighted by the factor $(\cos \alpha)^{-5/3}$. The final direction of the Cs^+ trajectory and the local surface normal direction determines

the angle α for each trajectory.

2.2.2 Sputtering yield vs. incident Cs^+-ion energy

The recent review by Andersen and Bay[11]) summarizes the available sputtering-yield data as a function of bombarding energy for many ions incident on more than 35 elements. By far most data correspond to energies below 1 keV and the most commonly employed ions have been those of hydrogen and the noble gases. Figure 4.38 of ref. 11 illustrates the independence of the sputtering yield on the projectile mass for few-keV heavy ($m_1 \gtrsim 50$) projectiles. Thus for materials on which sputtering yield data are not available for Cs^+ ions incident one can approximate the yield by data for other heavy projectiles such as Kr, Xe, Hg or Pb. Table 2 lists a few references containing data pertinent to the present problem. Note that inclusion of the sputtering yield in the calculation allows one to predict the beam current, but does not affect the calculated emittance because the path of an ion trajectory (neglecting space charge effects) is independent of the current associated with the trajectory.

2.2.3 Initial-energy spectrum of sputtered particles

An important feature of the sputtered negative ions is their energy spectrum because, from the standpoint of the emittance calculation, an ion's initial energy and direction determine its location in phase space. The collision cascade theory[12]) of sputtering predicts a E^{-2} dependence for the high energy portion of the spectrum where the sputtered particle energy E is much larger than the surface binding energy. Surface binding inhibits ejection at lower energies and leads to a prediction of a peak in the distribution below ~ 10 eV. Nelson[28]) reviews some theoretical treatments and experimental measurements of sputtered

particle energy spectra, but his discussion is restricted to incident energies above 20 keV. Jurela[29,30]) reported measurements of the positive and negative sputter yields for several materials bombarded by 40-keV Ar^+ ions. He observed two characteristic energy distributions. For one group of target materials that included Mg, Al, Co, Ag and Au the full widths at half maximum (FWHM) were about 20 eV, while for the second group that included Cu, Mn, Ni and Ta the FWHM was about 80 eV. Andersen[19]) suggests that the negative-ion energy distribution of material sputtered from cesium-coated surfaces should be close to that of the neutrals from clean surfaces. Jurela[29]) noted that the energy distributions of sputtered negative ions had nearly the same shape as those of positive ions except at the highest energies where the negative-ion yield fell more sharply. Since the differences among the energy spectra of sputtered neutrals, positive ions and negative ions do not appear to be great, and since much of the available data is for positive-ion distributions we used results from both positive- and negative-ion measurements to construct a plausible energy distribution.

Krauss and Gruen report[31]) energy spectra for Ti^+, W^+, WO^+ and WO_2 sputtered by 2-keV Ar^+ ions and Na^+, Mo^+ and W^+ ions sputtered by 2-keV O_2^+ ions. The distribution for Ti^+ peaks at ~ 10 eV and has a FWHM of about 45 eV. More than 60% of the Ti^+ ions have energies greater than 19 eV[31]). The situation is similar for the Na^+, Mo^+ and W^+ sputtered ions with very pronounced high-energy tails but with maxima at 1 eV, 14 eV and 35 eV respectively. Krauss and Gruen also describe[32]) the energy distribution of aluminum ions sputtered by 0.5- to 2.5-keV Ar^+ ions incident at 65° to the normal direction. The peak Al^+ yield shifts from ~ 5 eV at an Ar^+ energy of 0.5 keV to ~ 20 eV at 2.5 keV, but the shape

of the distribution beyond a sputtered energy of 25 eV is similar for all incident energies. For 2.5-keV incident Ar^+ ions the yield curve does not fall to 10% of the peak yield until the Al^+ energy exceeds 50 eV.

Doucas[20,33]) has made careful measurements of the energy spread of the 20-keV negative-ion beam from a Middleton-type sputter cone source. These measured distributions have long high-energy tails and FWHM of the order of 10-12 eV and the distributions resemble the spectra of sputtered neutral atoms. The exact energy of the peaks in the distributions was difficult to determine because of difficulties with the retarding field analyzer[20]). One must not assume that the beam energy spread determined in this manner is the same as the energy spread of the sputtered particles themselves. The present calculations show that the ion source serves as an energy filter, both shifting the peak in the distribution to lower energies and narrowing the width of energy distribution (see section 4.7). The more energetic sputtered ions are less likely to be extracted unless they are initially directed toward the exit aperture of the ion source. This effect is even more pronounced for the sputter cone source because unlike the SNICS cathode the sputtering surface faces away from the exit aperture.

Veksler's[34]) measurements of sputtered particle energies correspond closely with the conditions present in the SNICS source. He measured sputtered positive-ion energy spectra for 0.9 to 2.15-keV Cs^+ ions incident on Mo and Ta. The mean sputtered energies were 21-23 eV for Mo^+ and 26-36 eV for Ta^+ and the widths of the energy distributions were 30-35 eV for Mo^+ and 35-50 eV for Ta^+. We assumed that the negative-ion energy spectrum resembles the positive-ion energy spectra reported

by Veksler. Lacking specific experimental data on the energy distribution for the different cathode materials used in SNICS we used the same energy spectrum for all of the emittance calculations reported below. However, we did investigate the effect on the calculated emittance of varying the shape of the distribution. The calculation is not very sensitive to the detailed shape or width of the energy spectrum. We compared two calculations which were the same in all respects except for the assumed energy spectrum of sputtered particles. In the first calculation the spectrum peaked at 20 eV and had a FWHM of 45 eV and in the second one the peak occurred at 25 eV and the FWHM was 70 eV. In both cases the distribution included no negative ions with initial energies higher than 100 eV. The 70-eV-wide spectrum had only a 2% to 7% larger emittance for 90% of the beam than the 45-eV-wide spectrum. Higher cathode voltages corresponded to larger increases in emittance.

2.2.4 Sputtered particle angular distribution

We confine the discussion to distributions from polycrystalline sputter targets. In reviews of this topic the measured distributions are often called either "under cosine" or "over cosine". These terms were first introduced by Wehner and Rosenburg[35]) to describe how the distribution differs from a purely cosine distribution. In an over-cosine distribution more particles are ejected normal to the surface than in a cosine distribution. Under-cosine distributions predominate for incident ion energies below about 1 keV while over-cosine distributions are common for energies of the order of 20 keV and higher. For the energy range of 2 to 5 keV most often encountered in the sputter source a simple cosine approximates reasonably well the angular distribution function for practically all materials and for a wide range of various other

physical parameters such as angle of incidence and temperature.

For an assumed cosine distribution of the current density of sputtered negative ions the computer code generates trajectories whose initial directions sample all possible initial directions. Consider a "local" spherical coordinate system (ϕ, ω, z_n) whose origin is at cylindrical coordinates (r, θ, z) on the cathode surface and where z_n is in the direction of the local surface normal. The angle of emission of a negative ion is the polar angle ϕ. We assume an equal likelihood for emission at any azimuthal angle ω around a cone of half angle ϕ. The current density varies as cos ϕ but the available solid angle varies as sin ϕ. Thus if each trajectory traced represents the same amount of negative ion current, the distribution of initial directions will be bunched around ϕ = 45°. To generate n initial directions between ϕ = 0 and 90° the program uses the recursion relation

$$\phi_{k+1} = \sin^{-1} \left[\left(\frac{1}{n} + \sin^2 \phi_k \right)^{1/2} \right]$$

where k = 1,2,... ,n and ϕ_1 = 0°. For each angle ϕ the program computes the initial velocity for a number of angles ω evenly distributed around a cone of half angle ϕ. Actually, because of the symmetry involved, the angle ω need only range between 0 and 180° where ω = 90° corresponds to the trajectory with the maximum angular momentum about the symmetry axis. Typically, a group of 50 to 100 trajectories generated in this manner for each initial position and energy has proved to be an adequate sampling.

3. Calculation procedure

The procedure we developed to calculate the beam's phase space brightness distribution and hence its beam current and emittance

involves four steps: 1) calculation of the electric potential for a chosen source geometry and cathode voltage, 2) calculation of the Cs^+-ion trajectories to determine the cathode sputter rate, 3) calculation of the negative-ion trajectories emerging from the cathode surface, and 4) construction of the phase space brightness distribution from the final positions and velocities of the negative ions. Three different computer codes perform these calculations, one each for steps (1) and (4) and a third program for steps (2) and (3). The following sections describe the principles of operation and the capabilities of these three programs. The routines run on the Cray-1S and Cray-1A machines operated by the National Magnetic Fusion Energy Computing Center at Livermore, California.

3.1 Electric potential

The first step for a particular ion-source geometry is to calculate the electric potential in which the Cs^+ ions and sputtered negative ions move. Program DIRICH solves the Laplace equation (or the Poisson equation if space charge is included) in cylindrical coordinates and subject to Dirichlet boundary conditions (in which electric potentials are specified on conducting surfaces). Cylindrical symmetry is assumed so the potential need only be determined in a half plane from $r = 0$ to $r = r_{max}$. The Poisson equation in cylindrical coordinates is

$$\nabla^2\Phi = \frac{1}{r}\frac{\partial}{\partial r}\left(r\frac{\partial\Phi}{\partial r}\right) + \frac{1}{r^2}\frac{\partial^2\Phi}{\partial\theta^2} + \frac{\partial^2\Phi}{\partial z^2} = -\frac{\rho}{\varepsilon_o} \qquad (2)$$

where Φ is the electric potential in volts, ρ is the space charge density in C/m^3 and $\varepsilon_o = 8.85 \times 10^{-12}$ F/m. Cylindrical symmetry implies that $\partial\Phi/\partial\theta = 0$ and thus eq. (2) reduces to

$$\frac{1}{r}\frac{\partial \Phi}{\partial r} + \frac{\partial^2 \Phi}{\partial r^2} + \frac{\partial^2 \Phi}{\partial z^2} = \frac{\rho(r,z)}{\varepsilon_o} \tag{3}$$

The simpler Laplace equation has, of course, $\rho = 0$. The program solves for the potential $\Phi(r,z)$ on a mesh of approximately 10^5 points using the method of successive over-relaxation (SOR)[36]. To save computation time, the program initializes the 10^5-point array by interpolating values from the solution on a coarser mesh of 6400 points. If space charge is included, the program uses an iterative method to arrive at a self-consistent set of representative ion trajectories and electric potential. The charge density $\rho(r,z)$ for each SOR procedure results from the ion trajectories calculated in the previous iteration's electric potential. Computation time depends upon the number of iterations needed to obtain a stable potential and stable ion trajectories.

Fortunately, for many of the ion-source configurations in which we are interested, there is reason to believe that the effects of space charge are small and may be neglected. The main effect of the slow-moving Cs^+ ions near the ionizer is to distort the equipotentials near anode potential. In a test case, even when we neglected the effects of thermal electrons (which would tend to neutralize Cs^+ space charge), the space charge of a 1-mA Cs^+ beam did not appreciably alter the calculated cathode sputtering rate. Sputtered negative ions are not affected by the Cs^+ space charge because they gain energy rapidly as they leave the cathode and this region contains only fast Cs^+ ions (and hence no appreciable positive space charge). Of course, for large negative-ion currents, mutual repulsion may eventually lead to increased emittance. However, we have not included the effects of space charge in most of the calculations with the

intention of eliciting as much information as possible about ion-source systematics without excessively long computation times. Neglect of space charge effects will be a prime suspect as a possible cause of disagreement between measurements and calculation should such disagreement arise.

3.2 Particle trajectories

Program PTRAC calculates the trajectory of a charged particle using a sixth-order Runge-Kutta method. The potential consists of a rectangular array of equal-sized cells with the magnitude of the electric potential specified on the corners of the cells. The program transports the particle from one cell wall to another until the particle either collides with a solid surface or emerges from the exit aperture of the ion source. The original version of PTRAC written by D. Wiltzius for the National Electrostatics Corporation used relativistic equations for motion in a plane. The program was used mainly for tracing electron trajectories that start with nearly zero energy and accelerate to hundreds of keV. In a cylindrically symmetric potential $\frac{\partial \Phi}{\partial \theta} = 0$, and hence particles with practically no initial energy also have no initial angular momentum and they cannot acquire angular momentum. The motion is confined to the (r,z) plane. In our application the velocities are strictly nonrelativistic since we are interested in the trajectories of massive particles up to energies of a few keV. However, the initial angular momentum of the relatively energetic sputtered negative ions cannot be ignored. Consider a sputtered ion whose initial velocity does not lie in the (r,z) plane. The trajectory of such a particle spirals about the symmetry axis with constant angular momentum. As the particle accelerates in the z direction all of its acquired energy appears as translational kinetic energy, but

as it accelerates in the r direction some of the energy appears as rotational energy subject to the constraint that the angular momentum about r = 0 is conserved.

To allow for the possibility of particles with angular momentum a modification of the equations of motion used in PTRAC was necessary. The Runge-Kutta algorithm[37]) solves equations of the form:

$$\frac{du}{dz} = u' = f(r,z,u) \tag{4}$$

where u is the slope of the trajectory

$$u = \frac{dr}{dz} = r'. \tag{5}$$

Equation (4) has the following form for the case of a particle with angular momentum L

$$u' = \frac{\gamma(1+u^2)}{m_o c^2(\gamma^2-1)} \left[qE_r + \frac{L^2}{m_o \gamma r^3} - quE_z\right] \tag{6}$$

where m_o is the particle's rest mass, q is its electric charge, E_r and E_z are magnitudes of the electric field components and $\gamma = (1-v^2/c^2)^{-1/2}$. The fact that a trajectory with nonzero angular momentum executes a spiral path is not important for the present calculations because the resultant distribution of final particle coordinates will be integrated over the azimuthal angle θ and the assumption of cylindrical symmetry makes this integration trivial. The PTRAC routine need not keep track of the particle's current azimuthal coordinate. In effect, we trace the particle's path in an (r,z) plane that rotates about r = 0 at the particle's azimuthal velocity.

3.3 Calculation of emittance

Program PSPACE constructs the beam's phase space current density (or brightness) distribution from a set of representative negative-ion trajectories. One integrates this brightness distribution within a particular closed contour C of constant brightness to find the portion of the total current contained within C:

$$I = \iint_C B(x,x')dx\,dx' \tag{7}$$

Integration over all the available phase space, of course, yields the total beam current. The phase space area occupied by the current I is given by

$$A = \iint_C 1\,dx\,dx'. \tag{8}$$

The normalized emittance is

$$E = (A/\pi)E^{1/2} \tag{9}$$

where E is the energy of the beam with brightness distribution B(x,x').

In our numerical model we subdivide a portion of the positive-position half of (x,x') phase space into a 50 × 50 array of cells. The computer code PSPACE selects the cell size and location of the phase space origin for optimum resolution. Since the array contains the brightness distribution for the beam emerging from the ion-source exit aperture, the largest aperture diameter used in the calculation determines the width of a cell Δx in the position coordinate. The minimum and maximum divergence coordinates of the calculated negative-ion trajectories fix both the cell width $\Delta x'$ in the divergence coordinate and the number of cells used for positive and negative divergence. A typical calculation uses a 0.68 mm × 6 mrad

cell with about two thirds of the cells corresponding to positive divergence (reflecting the fact that the beam is generally diverging at the exit aperture).

After the dimensions of the phase space array have been established one accumulates into the array the beam current associated with each negative-ion trajectory. Next to calculating the representative trajectories this is the most time consuming part of the calculation. From a set of a few thousand calculated negative-ion trajectories the PSPACE program generates final position and divergence coordinates and the associated beam current for about a million negative ions. Calculated trajectories are characterized by their initial position, energy, and direction and by their final phase space coordinates. A relatively sparse sampling of trajectories for a few values of the initial position and energy provides enough information to infer by interpolation the final phase space coordinates in fine steps over the range of initial positions and energies. The program calculates the beam current associated with these interpolated trajectories from normalized probability distributions for each of the various effects discussed above that influence the sputter yield. Each trajectory generated in this manner contributes its current to a group of up to four neighboring cells in the phase space array. The current is divided among the cells according to the proximity of the trajectory to the centers of the nearest cells. The average cell in the array receives contributions of current from several hundred different trajectories and hence results in statistical fluctuations of the order of a few percent.

At this point in the calculation we perform an integration

over all possible azimuthal angles. Note that the brightness distribution $B(x,x')$ is defined in a rectangular coordinate system. (This is not the only possible definition. One could discuss the brightness distribution $B(r,r')$, for example, where r is the radial position in cylindrical coordinates. However, our emittance measuring device scans either (x,x') or (y,y') phase space. Thus to generate emittance results for comparison with experimental data we use $B(x,x')$.) In cylindrical coordinates each negative-ion trajectory has final position coordinates (r_f, θ_f, z_f) and final velocity $(\dot{r}_f, \dot{\theta}_f, \dot{z}_f)$. This particle's location in the (x,x') phase plane is $(r_f \cos\theta_f, r_f' \cos\theta_f)$ where $r_f' = \tan^{-1}(\dot{r}_f/\dot{z}_f)$. For a chosen aperture diameter the PSPACE program checks each calculated trajectory to see whether r_f lies within the aperture. If it does, then the program divides that trajectory's current equally among a large number of phase space locations (x, x') corresponding to a uniform distribution over angle θ_f (as implied by the assumption of cylindrical symmetry).

The next step in the calculation is to perform the numerical integrations indicated in eqs. (7) and (8) for several different equi-brightness contours C. This task involves scanning the array of cells and summing all the current in cells which contain more than the current $B_C \Delta x \Delta x'$ where B_C is the value of the brightness along contour C. The phase space area A is the number of such cells times the area of a cell $\Delta x \Delta x'$.

4. Results

The rest of the paper describes results of the trajectory and phase space calculations. We begin with a discussion of the Cs^+-ion trajectories and their relationship to the observed sputtering pattern

of the cathode. Next, we present a detailed account of the emittance results for a particular source configuration that had been in use for a long period of time. Predictions of the calculation will be compared with emittance measurements for this geometry which we call the standard SNICS geometry. Finally, we will discuss a source geometry that includes improvements made largely because of the calculation's predictions. More than fifty calculations have been completed for various geometrical configurations and computational techniques. The results presented here are highlights of the numerous calculations.

4.1 Cathode sputtering

Figure 3 is a scanning electron micrograph of an aluminum cathode. After several days of running we removed the cathode and cut it through the symmetry axis in order to show the erosion pattern in cross section. This erosion pattern is characteristic of all sputter sources of this type and, indeed, provides the most direct evidence that the Cs^+ ions incident on the sputter cathode surface are fast ions that come directly from the hot W ionizer. The results of a calculation of the electric potential are shown in fig. 4 which also illustrates 125 sample Cs^+-ion trajectories out of a total of 1250 trajectories that were calculated. The computer program assigns an amount of current to each of the trajectories in such a way that an equal amount of Cs^+-ion current emerges from each unit area of the tungsten ionizer. Not all of the Cs^+ ions that emerge from the ionizer eventually reach the cathode. A few of the trajectories that we trace end on another portion of the ionizer or on some other electrode at anode potential. For the geometry shown in fig. 4 about 97% of the calculated trajectories

strike the cathode, but for some of the other configurations discussed below the ratio is between 85 and 90%. We have no way to determine experimentally this collection efficiency of the ion source. We usually measure the total current between the ionizer (at anode potential) and the sputter cathode. This current includes Cs^+ ions incident on the cathode as well as negative ions and electrons emitted by the cathode. Under ordinary conditions the Cs^+ component is typically about half of the total sputter cathode current. For making comparisons among different source geometries we chose to normalize all of the results so that they correspond to 1 mA of Cs^+ current incident on the cathode.

One of the first things we calculated from the trajectories shown in fig. 4 was the effective Cs^+-ion current density on the face of the sputter cathode. Since we were interested in the Cs^+ beam's effect on sputtering the surface, we weighted the current by the angular dependence of the sputtering shown in fig. 2. Figure 5 shows the calculated Cs^+-ion current density weighted by impact angle as a function of the radial position along the cathode of fig. 4. This current density may be regarded as the effective Cs^+ current density if all the particles were incident normal to the surface. Displayed in this manner the results for other source geometries may be compared directly with fig. 5. Of the total 1-mA Cs^+ beam incident on the cathode 0.514 mA hit the face of the cathode while the remaining 0.486 mA hit the side. Weighted by impact angle the effective Cs^+ current on the face of the cathode is about 50% higher or 0.783 mA.

The shape of the curve in fig. 5 explains immediately the most obvious feature of a cathode's erosion pattern, the deep axial hole (see fig. 3).

However, the calculation also helps to explain, at least qualitatively, other aspects of the erosion pattern. The peaks in the current density near 1-mm radius and between 2 mm and 3 mm would with perfect cylindrical symmetry result in the erosion of circular grooves on the face of the cathode. The peaks result from a weak electrostatic focussing of the Cs^+ trajectories emerging between successive hoops of the ionizer (see the equipotentials in fig. 4). The actual helical shape of the ionizer causes a shift in the location of the radial peaks as a function of the azimuth angle and leads to a spiral rather than a circular groove.

Figure 4 shows that almost half of the Cs^+ ions produce unwanted sputtering of the side of the cathode and correctly predicts the erosion on the side of the cathode shown in fig. 3c. An improvement in the ionizer efficiency would involve redirecting these ions onto the cathode face. We calculated trajectories for a few modifications of the original geometry and found that the simplest solution was to move the cathode so that it was no longer inside the ionizer and insert an aperture at anode potential between the ionizer and the cathode. This configuration, shown in fig. 6, delivers 100% of the available Cs^+-ion current onto the cathode face. Figure 7 shows the effective Cs^+ current density for this geometry. While the peak current density is twice that of the original geometry (see fig. 5) the total weighted current is only about 43% higher because a larger portion of Cs^+ ions strike the surface at angles close to normal incidence. This prediction still represents a substantial improvement, however, and when we made the changes to the ion source, we did measure a higher negative-ion current per unit sputter cathode current than we obtained previously. The presence of the aperture

between the ionizer and the cathode had the added advantage of eliminating a problem with the alignment of the ionizer helix. (This effect cannot be modelled by the calculation since the helix does not have cylindrical symmetry.) We had observed that optimum performance of the source occurred when the helix was positioned slightly off axis to compensate for a steering effect of the pitch in the helical winding. With the geometry of fig. 6 the aperture has cylindrical symmetry and provides for a cylindrically symmetric electric potential in the region where the negative ions attain ~ 75% of their final energy. Thus the alignment of the ionizer helix was made less critical.

4.2 Negative-ion trajectories

Figure 8 displays a few samples of the calculated negative-ion trajectories for the same source geometry shown in fig. 6. The program calculated 7700 trajectories corresponding to 10 initial locations along the cathode face, 10 initial energies and 77 initial directions. The 400 trajectories shown here include samples at all 10 initial locations but for only 2 of the initial energies and 20 of the initial directions. The reason that only a few of the trajectories appear to cross the axis of symmetry is that most of the trajectories were emitted from the surface in a direction out of the (r,z) plane which gave them angular momentum about the symmetry axis. The figure shows only the path of each particle in an (r,z) plane that moves with the particle at its own θ velocity. The few trajectories that cross the symmetry axis were emitted with an initial θ velocity (and hence angular momentum) of zero. For calculating the emittance the program stores the position and velocity that each negative ion has when it reaches the plane of the source exit aperture (at the top in fig. 8).

4.3 Emittance

Table 3 is a summary of the results of an emittance calculation for the source geometry of fig. 6 and for a 3-kV sputter-cathode voltage and 3-mm-diameter exit aperture. The beam currents listed in the third column correspond to a Ni^- beam produced by a 1-mA Cs^+ current on the cathode and an assumed negative-ion fraction of 2%. Figure 9 illustrates the contours of equal brightness that are listed in the leftmost column of table 3. The maximum brightness occurs at the phase space origin and the innermost contour corresponds to 50% of the maximum. The outermost contour corresponds to 0.1% of the maximum brightness. The heavy-lined brightness contour encloses 90% of the total beam current and corresponds in this case to about 4.5% of the maximum brightness. (For clarity, contours near the 90%-of-beam contour are often not plotted. In fig. 9 the two contours listed in table 3 that bracket the 90% contour have both been omitted.) Note that the 10% brightness contour encloses not 90% but only about 71% of the total beam current. This is typical of measurements of the SNICS emittance.

The shaded rectangle in the upper left-hand corner of fig. 9 indicates the size of an averaging window that the computer code uses to simulate the effect of the resolution of our emittance scanning device[38]. We measure beam emittance by electrostatically deflecting the beam across a pair of narrow slits after the beam has been accelerated to 25-35 keV. This system continuously samples a parallelogram-shaped region of phase space about 1 mm × 2.8 mrad. For a few-keV beam emerging from the exit aperture of the source a 0.2-mm × 20-mrad window provides about the same resolution as the emittance measuring device. The size of the

phase space cells used in the calculation (see section 3.3) are considerably smaller than this averaging window. Thus a "raw" phase space distribution may contain structure impossible to measure experimentally. The main effect of the averaging procedure is to smooth out statistical sampling fluctuations in the calculated array. It also, of course, mimics the observed instrumental effect of increasing the phase space enclosed by the very outermost contours.

The normalized emittance as defined by eq. (9) is invariant as the beam is accelerated to higher energies. Therefore, measurements of the emittance obtained for a ~ 30-keV beam may be compared directly with the calculated emittance listed in the right-hand column of table 3 provided, of course, that the ion source was operating under the same conditions that we assumed for the calculation. Figure 10 shows such a comparison in which the solid curve is the calculation result and the individual points are measurements. This agreement between experiment and calculation is typical for measurements obtained with relatively low (0.5-1.0 mA) sputter cathode current. We have found similar agreement of several other sets of measurements with their respective calculations for other cathode voltages between 2 kV and 5 kV. As the sputter cathode current exceeds about 5 mA the measured emittance tends to exceed the calculated emittance usually by less than 50% but occasionally by as much as a factor of 2. There are a number of effects that can result in an increased emittance. First, space charge effects cause expansion of both the sputtered negative-ion beam and of the incident Cs^+-ion beam as their respective current densities increase. In the case of the negative ions this mutual repulsion leads to a direct increase in the emittance of the beam. Mutual repulsion of the Cs^+ ions leads indirectly to

emittance growth of the negative-ion beam as the Cs^+ beam sputters a larger area of the cathode. Another important effect on the emittance is the changing shape of the cathode as sputtering erodes the surface. This effect increases emittance and is discussed in section 4.6. We mention it here to emphasize the fact that it is often difficult to maintain conditions in the ion source that correspond closely with the conditions assumed for a particular calculation.

Another effect that can influence the experimentally determined emittance involves Cs^+ ions formed on surfaces other than the W ionizer. The walls of the chamber surrounding the ionizer helix are of tantalum whose work function is large enough to surface ionize cesium. These Ta parts serve as radiation shields and may reach temperatures high enough to reduce the sticking probability of cesium so that continuous emission of Cs^+ ions is possible. These Cs^+ ions will also bombard the cathode and add to the negative-ion yield. We have seen erosion in regions of the cathode inaccessible to Cs^+ ions from the helical ionizer but within the line of sight from a hot Ta surface. If sputtered negative ions from these areas emerge from the source exit aperture they will necessarily increase the beam emittance.

The relative magnitude of most of these effects is difficult to determine. The results of fig. 10 indicate, however, that one can operate the ion source in a mode in which they are negligible. Thus the calculations represent the very best emittance that one can expect from the source and the actual measured emittance may be higher by as much as a factor of 2.

4.3.1 Emittance vs. cathode voltage

If space charge effects are negligible, the paths followed by charged particles in an electric field depend only on the ratio of the

particles' energy to the electric field strength. Consider the trajectory of a negative ion with an initial energy of 10 eV leaving the surface of a cathode held at -2 kV with respect to anode potential. If one changes the cathode voltage from -2 kV to -5 kV this 10-eV sputtered ion will, of course, follow a different trajectory. But a 25-eV sputtered ion from the same location and emitted in the same direction will follow a trajectory identical to the trajectory of the 10-eV ion in the 2-kV potential difference. The elapsed time of the two trajectories will be different, but the shapes of both trajectories and hence their final phase space position and divergence coordinates will be the same. We used this feature to calculate the phase space distribution for several cathode voltages from a common set of negative-ion trajectories.

The procedure may be summarized as follows. Let S(E) be the assumed sputtered-particle energy distribution and let V be the potential difference for which a complete set of negative-ion trajectories has been calculated. The initial energies of the calculated trajectories are E_1, E_2, ..., E_i,... . While filling the phase space array as described in section 3.3 for the cathode voltage V the PSPACE program determines the factor $S(E_i)$ for each trajectory and uses this value in the calculation of the current associated with the trajectory. To construct the phase space brightness distribution for any other cathode voltage V^* the program uses the factor $S(E_i^*)$ where $E_i^* = E_i(V^*/V)$. One samples the entire spectrum S(E) for all cathode voltages of interest by carefully choosing the energies E_i for the calculated trajectories. For most of the calculations, we were interested in cathode voltages between 2 and 5 kV. The function S(E) that we assumed was nonzero between E=0 and E=100 eV. If we calculate trajectories for a 2-kV potential difference the energies E_i

must range from 0 to 100 eV. Then, for example, by using the scaling procedure the subset of these trajectories with energies E_i between 0 and 40 eV samples the function S(E) for the 5-kV potential difference. Note that an exactly equivalent procedure would be to calculate trajectories with energies E_i between 0 and 250 eV for a 5-kV potential difference. In either case one obtains a denser sampling of S(E) for the lower voltage.

Figures 11 and 12 show brightness contours for cathode voltages of 2 and 5 kV, respectively. These plots correspond to the same source geometry as the 3-kV brightness distribution of fig. 9. These three figures illustrate a clear decrease in the phase space area for increasing cathode voltage. Nevertheless, the normalized emittance increases as a function of the cathode voltage because the $E^{1/2}$ factor in eq. (9) more than offsets the decline in area A. Figure 13 plots the normalized emittance for 90% of the beam as a function of cathode voltage for two different exit aperture diameters. If the energies of all sputtered ions were negligible compared to the potential difference (i.e. if $E_i \approx 0$) then all of the distributions of figs. 9, 11 and 12 would be identical and the normalized emittance would increase as the square root of cathode voltage. Instead, the energy spectrum of the sputtered ions causes the emittance to rise significantly less rapidly than $V^{1/2}$. The following empirical relationship approximates to within a few percent the emittance curves shown in fig. 13.

$$E = E_o V^P \tag{10}$$

where V is the cathode voltage in kV and E is emittance in π mm mrad $MeV^{1/2}$. For the 3-mm-diameter aperture we find $E_o = 2.59$ and $P = 0.335$ and for the 6.35-mm-diameter aperture $E_o = 4.88$ and $P = 0.362$.

In order to test experimentally the power-law prediction of eq. (10) we made a series of emittance measurements for 5 different cathode voltages in the range from 2.2 to 3.0 kV. One would prefer to span a larger range of cathode voltages for such measurements, but it was difficult to maintain nearly identical operating conditions over very wide voltage ranges during the time necessary to collect the emittance data. We choose to run with as low a sputter cathode current as possible to obtain an approximately 10-μA Ni^- beam at each cathode voltage. This procedure minimized the possible effects of space charge. By using relatively low voltages and low Cs^+ currents we also reduced the effect of the changing shape of the cathode surface from rapid erosion.

The measurements consisted of about 13 points for each of the five cathode voltages 2.2, 2.4, 2.6, 2.8 and 3.0 keV. The 3-kV data are shown in fig. 10 and the other four sets of measurements are very similar. Since none of the measurements for any of the different cathode voltages corresponded to exactly the same percent of beam as measurements for any other cathode voltage we could not directly compare individual data points. Instead we decided to fit a smooth curve through the set of data for one cathode voltage and then find the power P in eq. (10) that scales this curve to fit the other data sets as well. We rewrote eq. (10) in the form:

$$E = a_1 (\xi - a_2)^{a_3} V^P \tag{11}$$

where (100-ξ) is the percent of beam. The parameters a_2 and a_3 determine the shape of the emittance-vs.-percent-of-beam curve and a_1 is an overall normalization factor. The procedure we used to find the power P involved

two separate nonlinear least-squares fits to the measured data. In the first fit we treated the product $a_1 V^P$ as a single parameter (a_0) and adjusted a_0, a_2 and a_3 for the "best" fit to the data for a single cathode voltage. The second fit fixed a_2 and a_3 and adjusted only the parameters a_1 and P for the best fit to all of the data for all cathode voltages. We repeated this whole procedure a total of five times using the data for each cathode voltage in turn to determine a_2 and a_3. The procedure minimized χ^2 in each fit using the variable metric technique of Davidon, Fletcher and Powell[39]).

Table 4 summarizes the results of this analysis. We arbitrarily assigned an error of ±6% to the individual emittance measurements to calculate the chi squared per degree of freedom (χ^2) for each fitting procedure. The column headings χ_1^2 and χ_2^2 refer to the χ^2 for the two separate fitting procedures at each cathode voltage as described above. Except for the 2.4-kV measurements all of the individual emittance curves are described adequately by a power-law curve with $a_3 \sim 1.55$. However, even though the parameters a_1, a_2 and a_3 for the 2.4-kV curve differ considerably from those of the other cathode voltages the power P that scales this curve to best fit the rest of the data is approximately the same as for the other curve shapes. Note that the best fit to any individual shape does not necessarily produce the best fit to all of the data when scaled by V^P. The average of the power P weighted by χ_2^2 for the five separate analyses is 0.321. This value is 4.2% lower than 0.335 which was the prediction of the emittance calculation. The lowest value of P in table 4 is about 15% below the prediction and the highest value is 2.1% above the prediction. Figure 14 shows all of the measured

data scaled by V^P to correspond to a cathode voltage of 3.0 kV. We used the power P = 0.309 determined from the analysis with the 3.0-kV shape parameters. The solid curve is a plot of eq. 11 for the parameters in the last row of table 4.

4.3.2 Emittance vs. aperture diameter

To determine the beam emittance as a function of the source exit aperture diameter, the computer code constructs each brightness distribution in several stages. The first stage includes only those negative-ion trajectories that emerge from a 1-mm-diameter aperture. After calculating the beam current and emittance for several brightness contours as described in section 3.3, the program adds to the brightness distribution the contribution from an annulus surrounding the present diameter. This procedure continues until the aperture diameter reaches 6.35 mm. Figure 15 shows the emittance for 90% of the beam as a function of the aperture diameter for three cathode voltages. These results correspond to the standard geometry illustrated in fig. 6. The curves increase approximately linearly and they are in good agreement with our measurements of emittance for aperture diameters of 1.5 mm, 2.0 mm and 3.0 mm. The nearly linear rise results from the fact that the average spread in divergence remains about the same as the aperture size increases. Figure 16 shows the brightness contours for a 6.35-mm-diameter aperture.

4.4 Negative-ion current

As discussed in section 2 the calculation predicts the negative-ion beam current if one supplies known sputtering yields. All of the results for beam currents and average brightness reported here are for Ni^- beams and assume an incident Cs^+ beam current of 1 mA and that 2% of the sputtered particles emerge from the cathode as negative ions. The assumption

of a 2% negative-ion fraction leads to Ni^- beam currents of the same order of magnitude that one observes experimentally from the SNICS source, but we cannot make a direct quantitative comparison of the calculated beam current with experiment. However, the calculation does serve to illustrate the relative merits of different source geometries and operating parameters such as cathode voltage.

The results for the standard SNICS geometry are displayed in figs. 17 and 18. Figure 17 shows that the beam current increases roughly quadratically with aperture diameter at least up to a diameter of 6.35 mm. One expects this result if the plane of the exit aperture is uniformly illuminated by negative ions. Measured beam currents for all ion species qualitatively agree with this prediction. For similar operating conditions we did observe approximately a four-fold increase in the beam current after opening the source aperture diameter from 1.5 mm to 3.0 mm.

We define the average normalized brightness for 90% of the beam as:

$$B_{90} = \frac{I_{90}}{E_{90}^2}. \tag{12}$$

Because our calculation assumes cylindrical symmetry, emittance is the same in both the (x,x') and (y,y') phase planes, and we denote the normalized emittance for 90% of the beam in either phase plane by E_{90}. I_{90} is 90% of the total beam current. (Various definitions for average brightness have been presented in the literature. So that the reader may easily compare values presented here to brightness values reported elsewhere, we note the following definite example. For a total beam current of 1 μA we have I_{90} = 0.9 μA = 900 nA. If this beam has a

2-dimensional emittance of, say, 3π mm mrad $MeV^{1/2}$, then the normalized brightness according to eq. 12 is about 10 nA mm^{-2} $mrad^{-2}$ MeV^{-1}). For the standard SNICS geometry fig. 19 shows that the average brightness for a 3-mm-diameter aperture is slightly higher than for a 6.35-mm-diameter aperture and that neither depends strongly on the cathode voltage.

4.5 Improved source geometries

Even after the addition of the aperture shown in fig. 6 which optimized utilization of the Cs^+ current, the overall extraction efficiency of the source was still low when measured in terms of the fraction of the total negative-ion beam available that actually emerged from the exit aperture. For the standard SNICS geometry we have been discussing so far the calculation predicts an efficiency of about 6.6% for a 3-mm-diameter aperture and a cathode voltage of 2 kV. This efficiency rises to 8.2% as the cathode voltage increases to 5 kV. At the expense of doubling the emittance (see fig. 13) one can increase the efficiency to 22% and 27% at 2 kV and 5 kV respectively by opening the exit aperture diameter to 6.35 mm. For the standard geometry about 70% of the beam emerging from a 6.35-mm aperture has the same emittance as 90% of the beam through a 3.00-mm aperture. Thus one realizes approximately a 2.5-fold increase in useable beam current with this enlargement of the exit aperture. Unfortunately, this improvement is accompanied by a nearly five-fold increase in the flow of Cs vapor through the aperture into the region of the first acceleration gap (see fig. 1). Middleton[40]) found it necessary to heat the extract electrode (either with an active element or by thin-wall construction) to prevent the arcing that eventually results from condensation of Cs vapor on the electrode and insulators.

A different approach to improving the extraction efficiency is

to provide focussing of the negative ions. The simplest way to focus the negative-ion beam emerging from the sputter cathode is to make the cathode tip an immersion lens. White[41]) reported such an arrangement for the so-called inverted sputter source of Chapman[42]). Yntema and Billquist[43]) have adopted a similar sputter-cathode geometry for the Argonne National Laboratory version of the Chapman source. The inverted sputter source is very similar to SNICS in many respects. It differs from SNICS in the use of a hollow porous-tungsten ionizer rather than the helical filament for the production of the Cs^+ beam. The term "inverted" refers to Chapman's modification[42]) of Middleton's original sputter-cone source[44]).

We calculated trajectories and emittance for a number of cathode shapes including several with an immersion lens at the tip of the cathode. Figure 20 shows equipotentials and sample Cs^+ trajectories for one of the more successful configurations. Table 5 compares the extraction efficiency of this arrangement with the standard geometry of fig. 6. The extraction efficiency of the source with the immersion lens is much higher for all cathode voltages and aperture diameters. The efficiency with the lens for a 3-mm aperture is even higher than that of the standard geometry with a 6.35-mm aperture, especially for higher cathode voltages. Of course, the addition of the immersion lens also increases the extraction efficiency for the larger 6.35-mm aperture, but, as we will discuss below, the attendant increase in the emittance is a serious disadvantage.

Figure 21 shows brightness contours for the geometry shown in fig. 20. Compare fig. 21 with fig. 12 which shows the phase space dis-

tribution for the standard SNICS geometry for the same aperture diameter and cathode voltage. The increase in extraction efficiency and hence beam current, comes at the expense of some increase in the emittance. Figures 22 through 26 illustrate these effects more clearly. Figure 22 shows that the calculated emittance for 90% of the beam still grows nearly linearly with the diameter of the exit aperture, but the magnitude of the emittance exceeds that for the standard geometry (see fig. 15) by 50 to 60%. The acceptance of the Wisconsin EN tandem electrostatic accelerator ranges from 6 to 10 π mm mrad $MeV^{1/2}$ for terminal voltages of 2 to 6 MV respectively. One must expect substantially less than 90% transmission through this machine if the source of fig. 20 is equipped with a large diameter exit aperture. Note that the emittance for 90% of the beam shown in fig. 23 is of the order of 6-8 π mm mrad $MeV^{1/2}$ for a 3-mm-diameter aperture but it ranges from 10 to 15 π mm mrad $MeV^{1/2}$ for a 6.35-mm aperture. As discussed earlier for the standard geometry the curves in fig. 23 are also described by eq. (10). For the 3.0-mm-diameter aperture the appropriate equation is $\bar{\epsilon} = 4.12V^{0.402}$ and for the 6.35-mm-diameter aperture it is $\bar{\epsilon} = 8.02V^{0.360}$. Note that the power P does not change for the larger aperture but increases from 0.335 to 0.402 for the smaller aperture when the cathode is equipped with an immersion lens.

Figure 24 shows that the beam current is not only substantially higher than for the standard geometry (see fig. 17) but also that the current no longer increases quadratically with aperture diameter. This difference, of course, is a direct result of the focussing and demonstrates that the plane of the exit aperture is not uniformly illuminated by negative ions but rather that the ion distribution peaks on axis. Figure 25 plots the calculated current as a function of cathode voltage

for comparison with fig. 18. The average brightness for 90% of the beam is shown in fig. 26 and may be compared with a similar plot in fig. 19 for the standard geometry.

4.6 Effect of cathode erosion

Figures 27 and 28 show the dependence of the calculated emittance and current on the depth of a hole eroded in the face of the sputter cathode. The shape of the hole used in these calculations resembles closely the electron micrograph shown in fig. 3d. A hole depth of zero corresponds to the standard geometry of fig. 6. We did five other complete emittance calculations with the hole depth on axis scaled from 1.2 mm to 6.0 mm. The increase of emittance with hole depth illustrated in fig. 27 agrees qualitatively with an experimentally observed gradual increase in the emittance with running time. The operating time required to erode a 6-mm-deep hole in the cathode depends on the cathode material and on the Cs^+ beam intensity. Copper and nickel cathodes last a few hundred hours for modest (1-2 mA) Cs^+ currents. The initial rise in beam current followed by a more gradual decline (see fig. 28) also agrees qualitatively with observed source behavior.

An eroded hole in the cathode is in effect a weak immersion lens, and, therefore, one should expect results similar to those calculated for the geometry of fig. 20. Notice that the gaps between curves of different cathode voltage in fig. 27 widen as the hole depth increases. The deeper the eroded hole the more rapidly the emittance rises with cathode voltage. For comparison with the standard geometry (fig. 6) and the geometry of fig. 20 we used eq. 10 to parametrize the emittance for different hole depths. For a hole depth of 2.4 mm $\bar{E} = 3.27\ V^{0.43}$, and for a depth of 6.0 mm $\bar{E} = 3.59V^{0.48}$, both of these results corresponding to a 3.0-mm-

diameter exit aperture. The effects of the erosion are not as pronounced if the cathode initially has the shape of an immersion lens as in fig. 20.

4.7. Beam energy spectrum

In section 2.2.3 we mentioned that the energy spectrum of the extracted beam can be different from the energy spectrum of sputtered ions. As each brightness distribution is constructed the PSPACE program also accumulates the negative-ion current in small energy intervals. Figure 29 shows the resulting energy spectra for the standard SNICS geometry of fig. 6 and for a cathode voltage of 3 kV. The solid curve represents all of the negative-ion current leaving the sputter cathode while the other two curves show the energy distribution of the beam emerging from a 3.0-mm and a 6.35-mm aperture. The total beam available peaks at about 18 eV and has a FWHM of ~ 45 eV, yet the most probable energy of the ions emerging from 3.0-mm and 6.35-mm apertures is about 2 eV and 10 eV respectively for this source geometry.

Figure 30 shows a similar plot for the geometry of fig. 20 and it illustrates the much higher extraction efficiency of the immersion lens. The total beam curve in fig. 30 is nearly the same as the total beam curve in fig. 29 since the two calculations assumed the same sputtered particle energy spectrum. Slight differences in the total beam curves are from small variations in the distribution of Cs^+-ion current on the cathode for the two calculations. For a 3-mm aperture and a cathode voltage of 3 kV the extracted beam's spectrum peaks near 5 eV and has a FWHM of about 23 eV. For a 6.35-mm aperture the spectrum more closely resembles the total beam spectrum since about 77% of the available beam is extracted. Nevertheless the peak occurs at 16 eV, slightly below

the peak in the total beam spectrum, and the FWHM is about 38 eV.

5. Discussion

The source lifetime T is the time required to sputter away all of the useable cathode material while maintaining the desired average output current of a particular beam species. If we consider the simplest case of a cathode made of an elemental material and allow for the possibility of various molecular beams in addition to the monatomic ion beam, we can define the lifetime as

$$T = \frac{\eta \mu f^{-} q N_A \rho V}{n_m I A} \tag{13}$$

where V is the total volume of cathode material sputtered,

ρ is the material's density,

A is the material's atomic number,

N_A is Avagadro's number (6.023×10^{23} atoms/mole),

I is the extracted average electrical current of the beam species with n_m atoms per ion,

q is the ionic charge,

μ is the fraction of all atoms that appear in the molecular (or atomic) beam of interest,

f^{-} is the fraction of those molecules (or atoms) that are negatively charged, and

η is the extraction efficiency of the ion source.

One operates the source with sufficient Cs^{+} beam incident on the cathode to obtain the current I. For a nickel cathode we find $\mu \approx 0.85$ for the sum of all of the monatomic isotopes. A typical extraction efficiency is $\eta \sim 0.3$ when using a focussing cathode and we had earlier estimated ~ 0.02 for f^{-}. If the source produces about 10 μA of Ni^{-} until 0.1 cm^3

of the cathode has been removed, then eq. 13 predicts a lifetime of 200 hours. This result is consistent with observed cathode lifetimes.

It is clear from the results of the calculations and measurements that obtaining a suitable beam from the sputter source for injection into a tandem accelerator involves a number of tradeoffs. The ideal mode of operation depends on the application and on how much emphasis is placed on reliability and lifetime. For example, from the emittance calculations one learns that for best emittance one should use as small an exit aperture and as low a cathode voltage as possible which still provides adequate beam current. Reducing the aperture diameter, however, reduces the extraction efficiency and hence also the source lifetime according to eq. 13. Materials such as boron that do not sputter readily require higher cathode voltages ($\gtrsim$ 5 kV) for effective operation.

Generally speaking our results for beam intensity with different cathode materials in the SNICS source are consistent with those of Middleton[4,40]) particularly if one takes into account the use of a much larger exit aperture in the Middleton source. We see essentially the same spectrum of carbon molecular negative ions as Middleton[40]). Results for B^- and B_2^- beams with cathodes sintered from mixtures of boron and aluminum powders also confirm Middleton's observations. Sintered AlB_2 powder also produces intense B^- and B_2^- beams. We have not yet had a demand for the monatomic Al^- beam, but we have used the Al_2^- beam extensively for radiation damage studies. For low cathode voltages (~ 2 kV) the ~ 8-μA Al_2^- is the only appreciable beam that we observe. Middleton[40]) produces 5-7 μA of Al^- by operating at high cathode voltage (6 kV) and high cathode current (7.5 mA), but the Al_2^- beam of 40 μA still dominates the spectrum. Beam intensities from both the

Wisconsin and the Pennsylvania sources for other materials such as copper, nickel and iron also scale as expected.

Middleton's estimate[40] of ~ 1.6 π mm mrad $MeV^{1/2}$ for the emittance of 70% of the beam from his source seems low by at least a factor of 3. His estimate was based upon the assumption that 80% of the beam originates within a 1-mm-diameter region of the cathode. The photograph of an eroded cathode in fig. 15 of ref. 40 is virtually identical to our fig. 3a, both showing considerable sputtering outside of the deep central pit. By calculating the volume of material sputtered from within various diameters for this typical erosion pattern we find that less than 5% of the beam originates within a diameter of 1 mm. Larger fractions of 20%, 50% and 80% of the total beam correspond to diameters of 2.4, 4.6 and 6.7 mm respectively. Based upon our trajectory calculations the source of ref. 40 with a cathode voltage of 5 kV should have an emittance for 70% of the beam between 4.7π and 6.3π mm mrad $MeV^{1/2}$ depending upon whether or not a focussing cathode geometry is used. The 90% emittance would be higher yet by about a factor of 2.

There are, of course, still other ways to improve SNICS and similar sputter sources. The maximum beam divergence is roughly proportional to the sum of the exit aperture diameter and the size of the Cs^+ beam spot on the cathode. Hence if the Cs^+ beam spot can be reduced, then the emittance will be improved. Our calculations predict that certain conically shaped ionizers should produce a better focussed Cs^+ beam. National Electrostatics Corporation has observed increased negative-ion current and good transmission of B^- beams using a conically shaped ionizer[45]. However, experimental emittance tests have not shown

the expected reduction in beam emittance for reasons that are not yet fully understood. We suspect that the effect is masked by negative-ion current sputtered by Cs^+ ions originating from hot surfaces other than the tungsten helix. For a substantially reduced Cs^+ beam spot though, the improvement in emittance would be accompanied by a degradation of the lifetime because of a smaller available volume of cathode material to sputter. If all of the sputtering were confined to a diameter of 1 mm, for example, then the 200-hour lifetime mentioned above would be reduced to only 10 hours if all the cathode material is spent when the hole depth reaches 6 mm.

Finally, we mention a word of caution about comparing our calculated emittance results with the acceptance of various accelerator systems. An important consideration is matching the shape of the beam emittance to the acceptance of the beam transport system[1,46]. Phase space matching is less important for very low emittance beams ($\lesssim 3\ \pi$ mm mrad $MeV^{1/2}$), but it becomes crucial as the beam emittance approaches the acceptance of the system. A typical tandem accelerator's acceptance is of the order of 8 π mm mrad $MeV^{1/2}$, though it has been made much higher in some systems. Larson and Jones report[46], for example, that a quadrupole triplet lens in the low-energy beam tube increased the acceptance of the Oak Ridge National Laboratory's folded tandem to $\sim 17\ \pi$ mm mrad $MeV^{1/2}$. Beam transport codes usually deal with elliptically shaped phase space areas since ellipses transform to other ellipses as the beam propagates in the absence of aberations and other nonconservative forces. The phase space areas reported here, however, generally have more complicated shapes (see for example figs. 16 and 21). An ellipse circumscribed around (say) the 90% brightness

contour might enclose substantially more area than the contour itself.

6. Conclusions

A very simple model in which only electrostatic forces play a role describes a wide variety of the negative-ion beam characteristics for SNICS and similar sputter-type sources. The computer simulation results are in good agreement with experimental measurements at least for Cs^+-ion currents up to ~ 1 mA and negative-ion currents of a few tens of microamps. For higher intensities the calculation provides a lower bound on the source emittance. The calculation serves as a useful tool in the development of new designs for higher beam current and lower beam emittance.

Acknowledgements

I wish to thank Professor Hugh T. Richards and Drs. Steven Riedhauser and Gregory T. Caskey for a number of invaluable suggestions and helpful discussions. I am also grateful to Daniel B. Bullen for preparing the electron micrographs; David Wiltzius and National Electrostatics Corporation for the computer code PTRAC; and Lori Wong of the National Magnetic Fusion Energy Computer Center for her assistance with the computer generated graphics.

REFERENCES

1) A.P. Banford, *The Transport of Charged Particle Beams* (Spon, London 1966).

2) G.T. Caskey, R.A. Douglas, H.T. Richards and H.V. Smith, Jr., Nucl. Instrum. and Meth. 157 (1978) 1.

3) J.H. Billen and H.T. Richards, Proceedings of the Symposium of Northeastern Accelerator Personnel CONF-781051 (Oak Ridge, Tenn. 1978) 137.

4) R. Middleton, Proceedings of the Symposium of Northeastern Accelerator Personnel CONF-781051 (Oak Ridge, Tenn. 1978) 114; and R. Middleton, Proceedings of the Symposium of Northeastern Accelerator Personnel (Madison, Wisconsin 1980) 134.

5) A. Kh. Ayukhanov and V.N. Chernenko, Pribory i Tokh. Éksperim. 15 (1972) 150 (Engl. Trans. Inst. and Exp. Tech 15 (1972) 480.

6) G.A. Norton and G.M. Klody, IEEE Trans. Nucl. Sci. NS-30 (1983) 1701.

7) R. Behrisch, Ergab. Exakten Naturwiss. 35 (1964) 295.

8) E.W. McDaniel, *Collision Phenomena in Ionized Gases* (Wiley & Sons, N.Y. 1964).

9) M. Kaminsky, *Atomic and Ionic Impact Phenomena on Metal Surfaces* (Academic Press, New York 1965).

10) G. Carter and J.S. Colligon, *Ion Bombardment of Solids* (American Elsevier Publishing Co., New York 1968).

11) H.H. Andersen and H.L. Bay in *Topics in Applied Physics*, Vol. 47 (R. Behrisch, ed. 1981).

12) P. Sigmund, Phys. Rev. 184 (1969) 383.

13) P. Sigmund, Rev. Roum. Phys. 17 (1972) 823.

14) P. Sigmund in *Topics in Applied Physics*, Vol. 47 (R. Behrisch, ed. 1981).

15) V.E. Krohn, J. Appl. Phys. 33 (1962) 3523.

REFERENCES (Cont'd)

16) H.V. Smith, Jr., Nucl. Instrum. & Meth. 153 (1978) 605.

17) M.L. Yu, Phys. Rev. Lett. 40 (1978) 574.

18) Ch. Lukner, Nucl. Instrum. & Meth. 167 (1979) 249.

19) H.H. Andersen, IEEE Trans. Nucl. Sci. NS-23 (1976) 959.

20) G. Doucas, Int. Journ. Mass Spectrometry and Ion Physics 25 (1977) 71.

21) P. Tykesson, H.H. Andersen and J. Heinemier, IEEE Trans. Nucl. Sci. NS-23 (1976) 1104.

22) H.L. Daley and J. Perel, AIAA Journ. 5 (1967) 113.

23) V.K. Koshkin, "Sergev Ordzhonikidze" Aerohauti Institut, Report (1975).

24) G.K. Wehner and D. Rosenberg, J. Appl. Phys. 32 (1961) 887.

25) K.B. Cheney and E.T. Pitkin, J. Appl. Phys. 36 (1965) 3542.

26) V.K. Koshkin, J.A. Rysov, I.I. Shkarban, and B.M. Gourmin, Proc. of the 4th Int. Conf. on Phenomena in Ionized Gases (North Holland, 1960) 92.

27) S. Ya. Lebedev, Yu. Ya. Stavisskii and Yu. V. Shut'ko, Soviet Phys. Tech. Phys. 9 (1964) 854.

28) R.S. Nelson, *The Observation of Atomic Collisions in Crystalline Solids*, (North-Holland, Amsterdam, 1968).

29) Z. Jurela, Rad. Effects 19 (1973) 175.

30) Z. Jurela, Int. Journ. Mass Specrom. and Ion Phys. 18 (1975) 101.

31) A.R. Krauss and D.M. Gruen, J. Appl. Phys. 14 (1977) 89.

32) A.R. Krauss and D.M. Gruen, Nucl. Instrum. & Meth. 149 (1978) 547.

33) G. Doucas, Revue Phys. Appl. 12 (1977) 1465.

34) V.I. Veksler, Soviet Physics JETP 11 (1960) 235.

REFERENCES (Cont'd)

35) G.K. Wehner and D. Rosenberg, J. Appl. Phys. 31 (1960) 177.

36) B.A. Carré, Comp. Journ. 4 (1961) 73.

37) W.E. Boyce and Richard C. DiPrima, *Elementary Differential Equations and Boundary Value Problems*, (Wiley and Sons, New York 1965).

38) L.L. Ames, Nucl. Instrum. & Meth. 151 (1978) 363.

39) R. Fletcher and M. Powell, Comp. Journ. 6 (1963) 163.

40) R. Middleton, Nucl. Instrum. & Meth. (to be published).

41) N.R. White, Nucl. Instrum. & Meth. 206 (1983) 15.

42) K.R. Chapman, Nucl. Instrum. & Meth. 124 (1975) 299.

43) J.L. Yntema and P.J. Billquist, Nucl. Instrum. & Meth. 199 (1982) 637.

44) R. Middleton and C.T. Adams, Nucl. Instrum. & Meth. 118 (1974) 329.

45) G.A. Norton, private communication.

46) J.D. Larson and C.M. Jones, Nucl. Instrum. & Meth. 140 (1977) 489.

Table 1

Definition of Symbols

Symbols	Definition
x,y,z	rectangular position coordinates
r,θ,z	cylindrical coordinates
x',y'	divergence coordinates
α	angle of incidence to surface normal
ϕ	angle of emission from surface normal
ω	azimuth angle in local coordinate system
E_r,E_z	electric field components
Φ	electric potential
ρ	charge density or mass density
ε_o	permittivity of free space
E	beam energy
I	beam current
A	phase space area
$\bar{\varepsilon}$	normalized emittance
B	brightness
V	cathode voltage
m_1	projectile mass
m_2	target mass
S	sputtering yield
f^-	negative ion fraction
L	angular momentum
q	electric charge

Table 1 (cont'd)

Definition of Symbols

Symbols	Definition
m_o	particle rest mass
v	particle velocity
c	speed of light
γ	relativistic factor $(1-v^2/c^2)^{-1/2}$
u	slope of trajectory

Table 2

Sputtering Yield Measurements for Low-energy Heavy Projectiles

Projectiles	Targets	Projectile Energy Range (keV)	Reference
Cs^+	Al,Cu,Ti	0.5-15	Daley and Perel[22])
$Kr^+Cs^+Xe^+Pb^+$	Fe, W	2-20	Koshkin[23])
Hg^+	Cu,Ni,Co,Fe, V,Ti,Ag,Pd, Rh,Mo,Au,Pt, Ta,W	4-15	Wehner and Rosenburg[24])
Xe^+	Cu,Mo,W	1.5-30	Cheney and Pitkin[25])
Kr^+Cs^+,Xe^+,Pb^+	Cu,Fe,Cd,Mo, W,Nb	1-20	Koshkin et al.[26])
Cs^+	C,Ti,Fe,Ni,Nb, Rh,Mo,Ta,W,Pt	2-10	Lebedev et al.[27])*

Footnote

* The Fe and Ni yields reported by Lebedev et al.[27]) generally agree with other available data, but the yields for the light target materials, C and Ti, are higher than other measurements by as much as a factor of 3 while the sputtering yields for heavier targets are lower than other measurements.

Table 3

Phase Space Contour Results for the Standard SNICS Geometry with a 3.0-mm Aperture and a 3.0-kV Cathode

Brightness Contour (% of max)	Percent of Beam	Beam Current (μA)	Phase Space Area (mm mrad)	Normalized Emittance (π mm mrad $MeV^{1/2}$)
0.0	100.0	6.95	606	10.57
0.1	99.9	6.94	454	7.92
0.5	99.5	6.91	393	6.84
1.0	98.7	6.86	353	6.15
2.0	96.9	6.73	304	5.30
3.0	94.4	6.56	266	4.64
4.0	91.6	6.37	235	4.10
4.5	90.0	6.25	221	3.85
5.0	88.4	6.14	208	3.63
6.0	84.7	5.89	182	3.17
7.0	81.3	5.65	162	2.82
8.0	77.5	5.38	142	2.48
9.0	74.7	5.19	129	2.26
10.0	70.9	4.92	113	1.98
12.0	65.1	4.52	93	1.63
15.0	58.4	4.05	74	1.28
20.0	49.5	3.44	53	0.93
30.0	33.2	2.31	27	0.47
40.0	20.9	1.45	14	0.24
50.0	14.1	0.98	8	0.13

Table 4

Fitted Parameters for Emittance

vs. Percent of Beam

Cathode Voltage	Parameters in Equation 11				Chi squared per degree of freedom	
	a_1	a_2	a_3	P	χ_1^2	χ_2^2
2.2	476	17.8	-1.52	0.284	0.91	2.42
2.4	1955	20.5	-1.87	0.318	1.07	1.29
2.6	516	14.1	-1.60	0.342	0.46	1.58
2.8	494	14.0	-1.59	0.341	0.64	1.53
3.0	469	15.6	-1.54	0.309	0.61	1.29

Table 5

Comparison of SNICS Extraction Efficiencies

Aperture Diameter (mm)	Cathode Voltage (kV)	Extraction Efficiency (%)	
		Standard Geometry	with Immersion lens
3.00	2.0	6.6	27
3.00	3.0	7.3	32
3.00	5.0	8.2	43
6.35	2.0	22	41
6.35	3.0	24	77
6.35	5.0	27	87

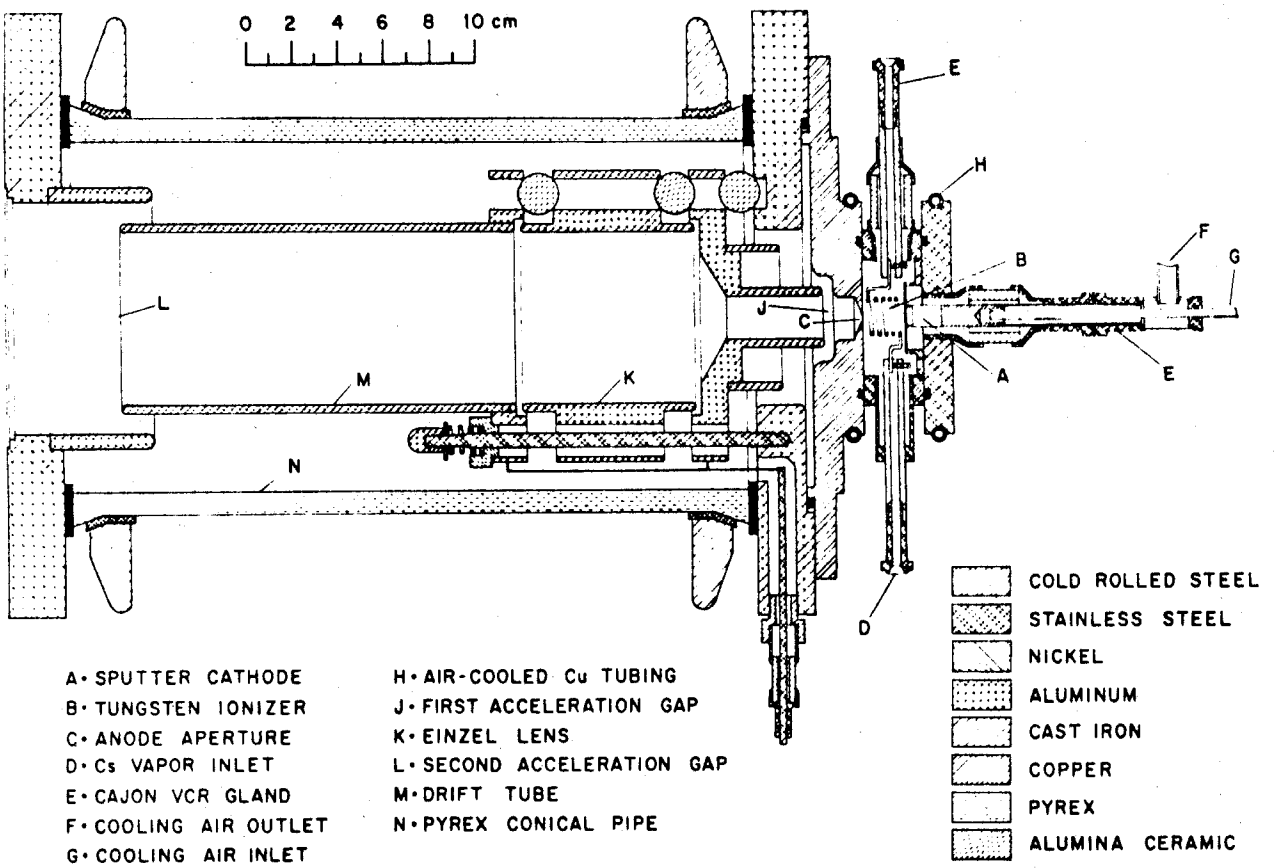

Fig. 1. Detail drawing of SNICS and acceleration and focus electrodes. The first acceleration gap (J) typically accelerates the beam by 5 keV and the second gap (L) by 20 keV. The total acceleration voltage is, therefore, 25 kV plus the cathode potential of 2 to 5 kV. Not shown are the Cs oven, the metering valve and the Ta heat shields around the ionizer (B).

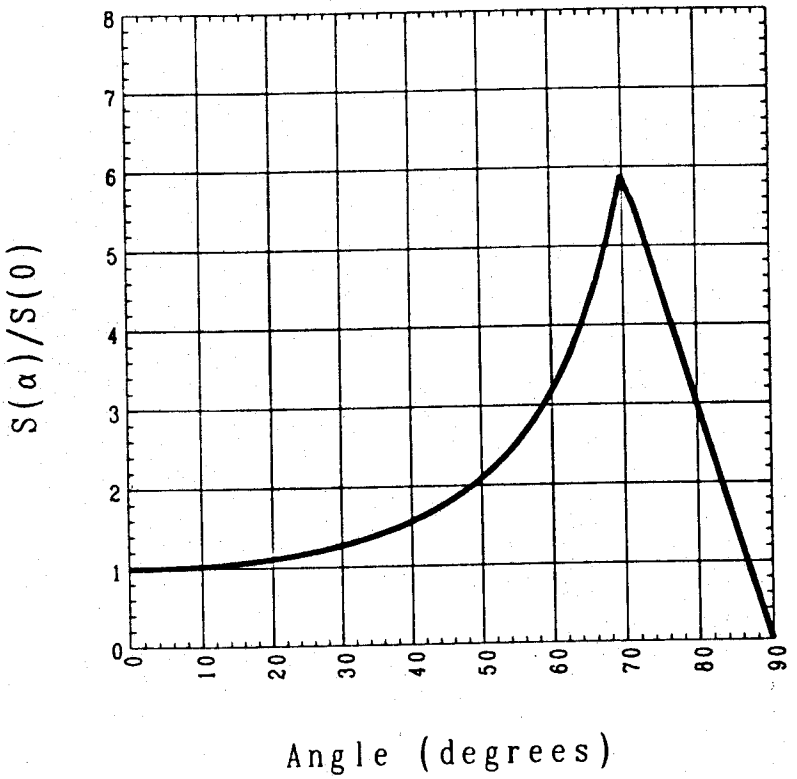

Fig. 2. Sputter rate vs. incident angle of Cs^+ ions assumed for the calculation. For angles $\alpha \leq 70°$, $S(\alpha)/S(\theta) = (\cos \alpha)^{-5/3}$ and for $\alpha > 70°$ we assume the sputter rate falls linearly to zero. Most of the Cs^+ ions strike the cathode at angles less than 60°.

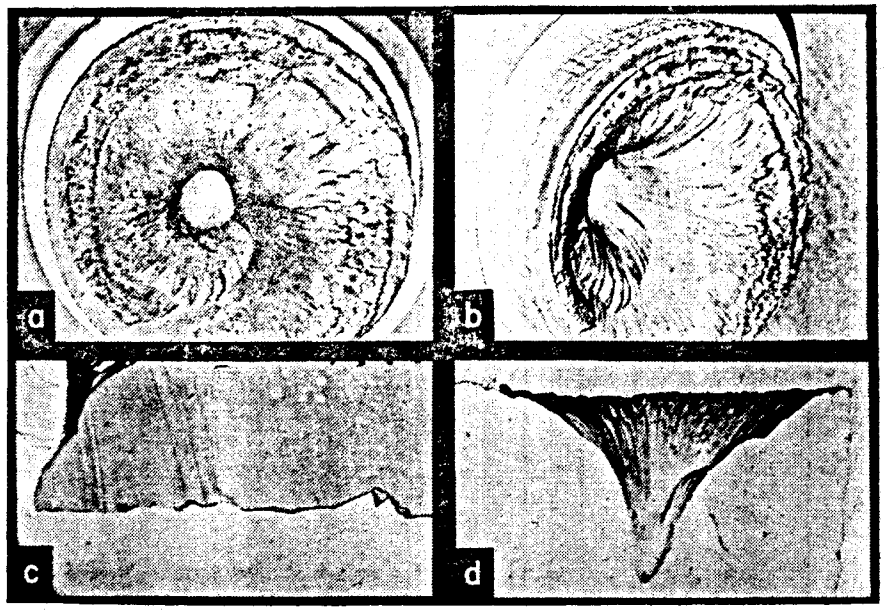

Fig. 3. Scanning electron micrographs of an aluminum sputter cathode after several days of running. The results are similar for cathodes of all other materials. This cathode was initially a rod 12.7 mm long by 9.5 mm in diameter. Part (a) shows a face-on view and (b) shows the cathode tilted 45°. Parts (c) and (d) show the cathode in cross section after it was cut through the symmetry axis. In (c) the front face is on the left and a groove eroded in the side is visible near the lower right. Part (d) shows the roughly conically shaped hole eroded in the face of the cathode.

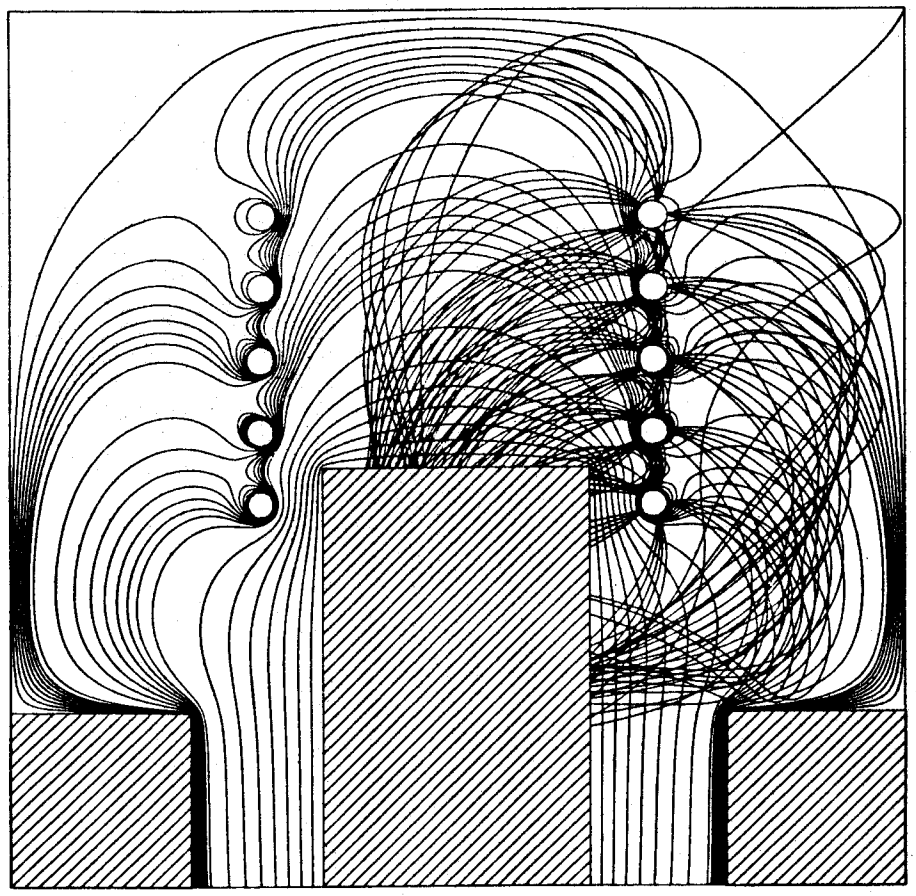

Fig. 4. Equipotentials and sample Cs^+-ion trajectories for the original SNICS geometry. The cathode in the center is several kV negative with respect to the ionizer and housing. Five circular hoops at anode potential approximate the 5-1/2-turn helical ionizer of 1-mm-diameter tungsten. Three groups of equipotential contours are shown. Successive contours nearest the sputter cathode differ in potential by about 11% of the total potential difference. Those in the next group differ by 1.1%, and the last group by 0.11%. One-tenth of the 1250 calculated trajectories appear here emerging from the W ionizer.

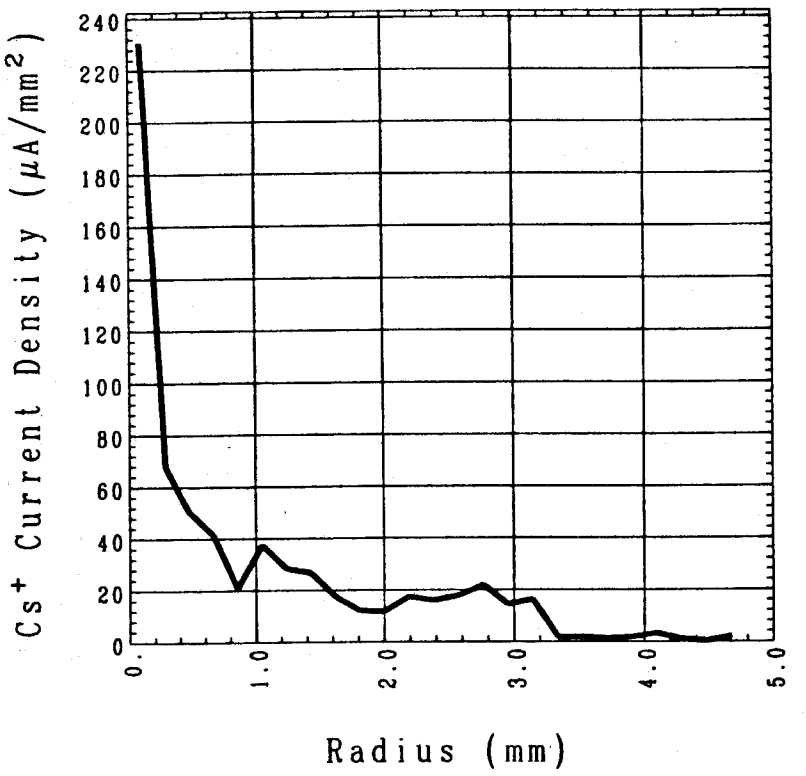

Fig. 5. Effective Cs^+ current density vs. radial position along face of cathode. This curve corresponds to the geometry shown in fig. 4 and assumes a 1-mA total Cs^+ current. It correctly predicts the enhanced axial erosion of the cathode displayed in fig. 3.

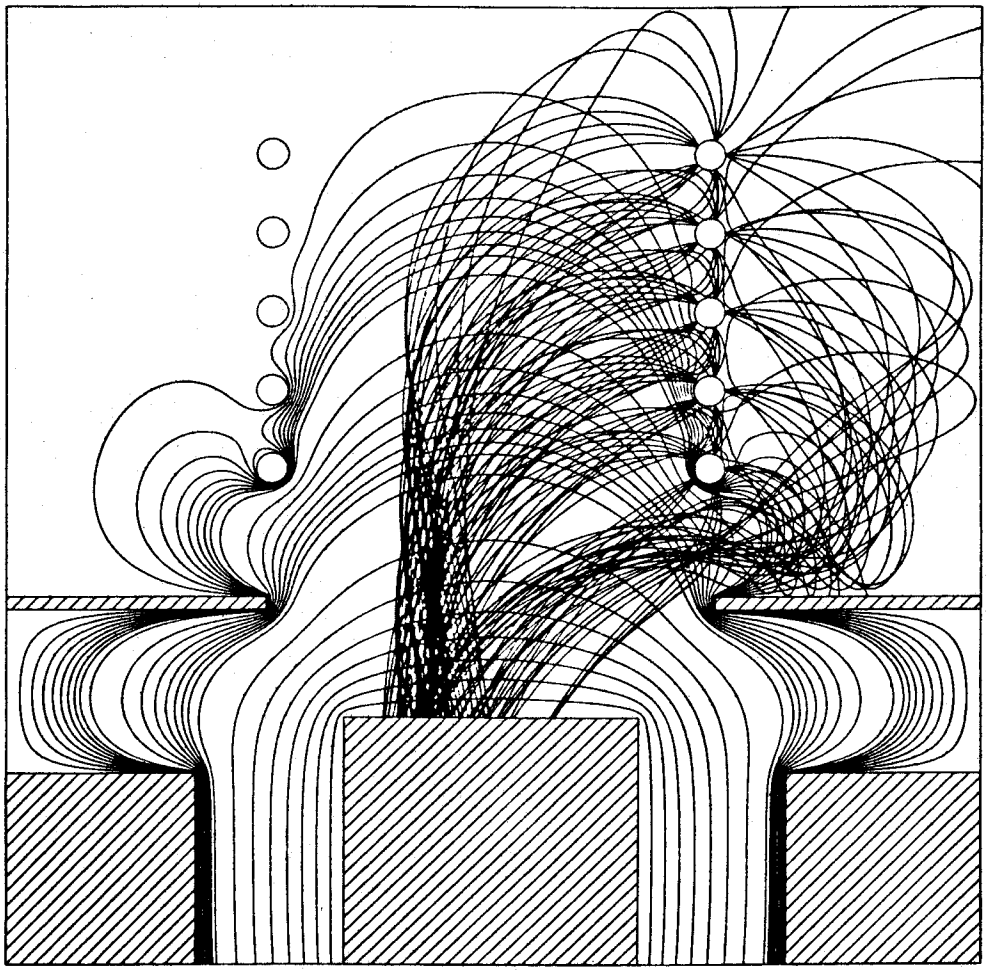

Fig. 6. Equipotentials and sample Cs^+-ion trajectories for an improved SNICS geometry. The aperture at anode potential between the ionizer and the cathode prevents Cs^+ ions from striking the side of the cathode and hence makes more efficient use of the available Cs^+-ion current. The equipotential contours correspond to the same voltages as those in fig. 4.

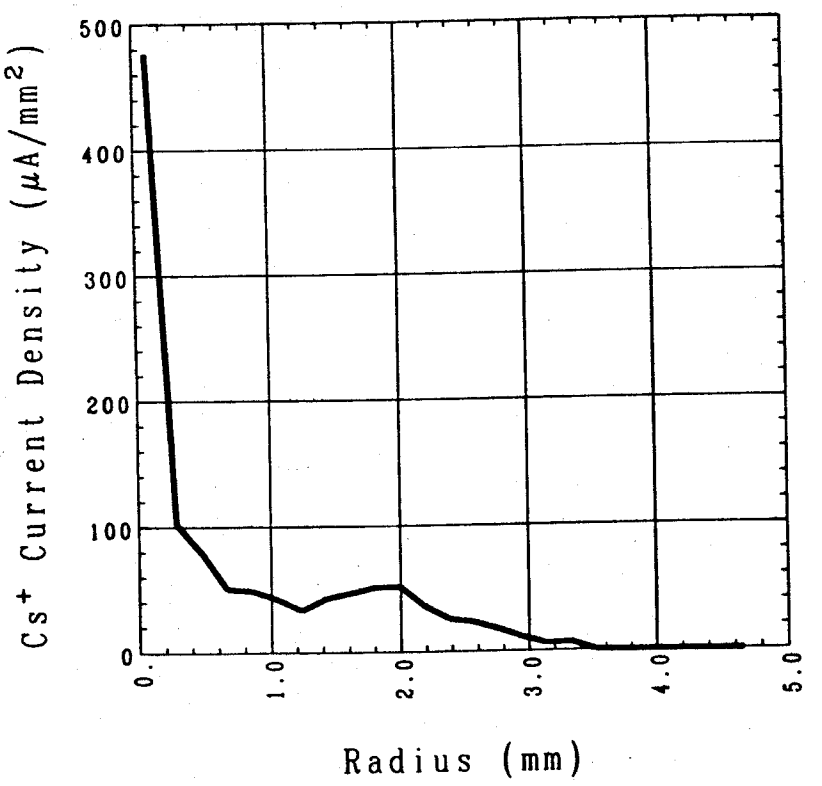

Fig. 7. Effective Cs^+ current density for the geometry of fig. 6. This curve and the curve in fig. 5 both correspond to a 1-mA total Cs^+ beam current. However, the on-axis current density shown here is about twice that of fig. 5.

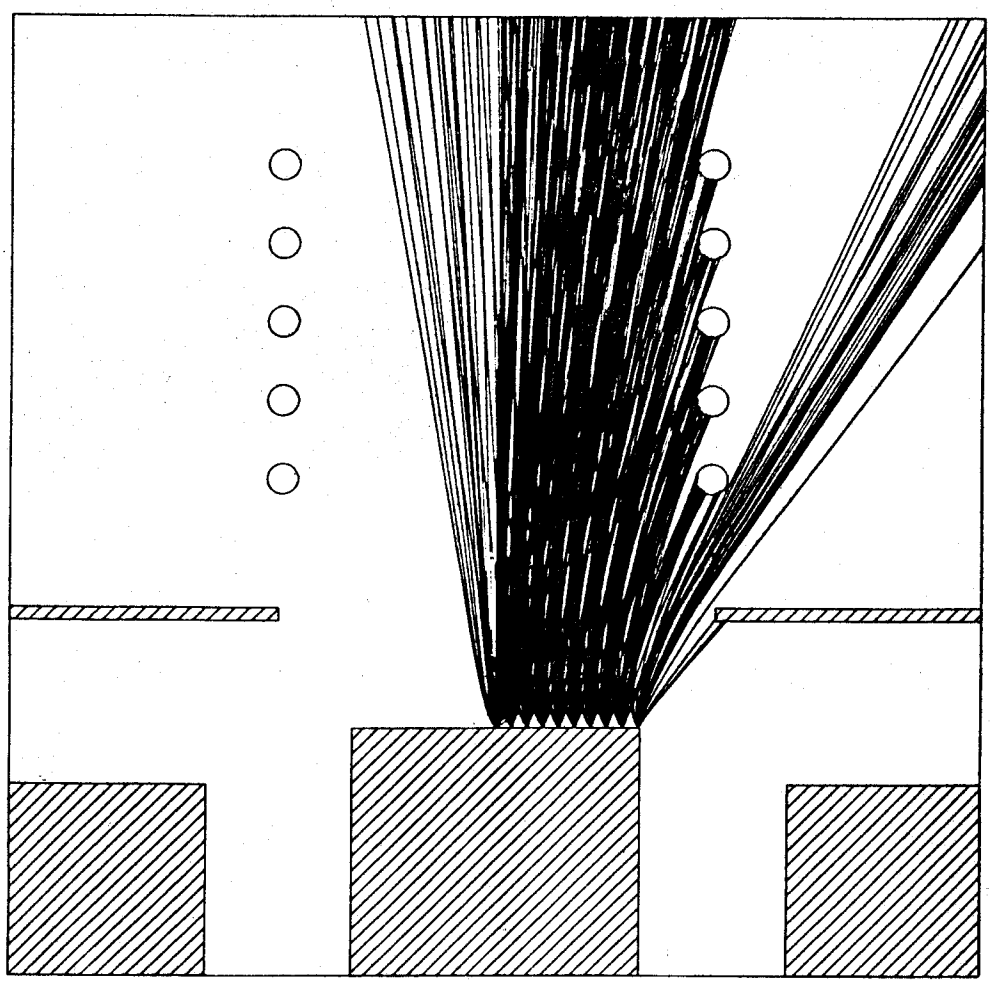

Fig. 8. Sample negative ion trajectories. About 5% of the 7700 calculated trajectories are shown here leaving the sputter cathode and accelerating toward the plane of the source exit aperture at the top of the figure.

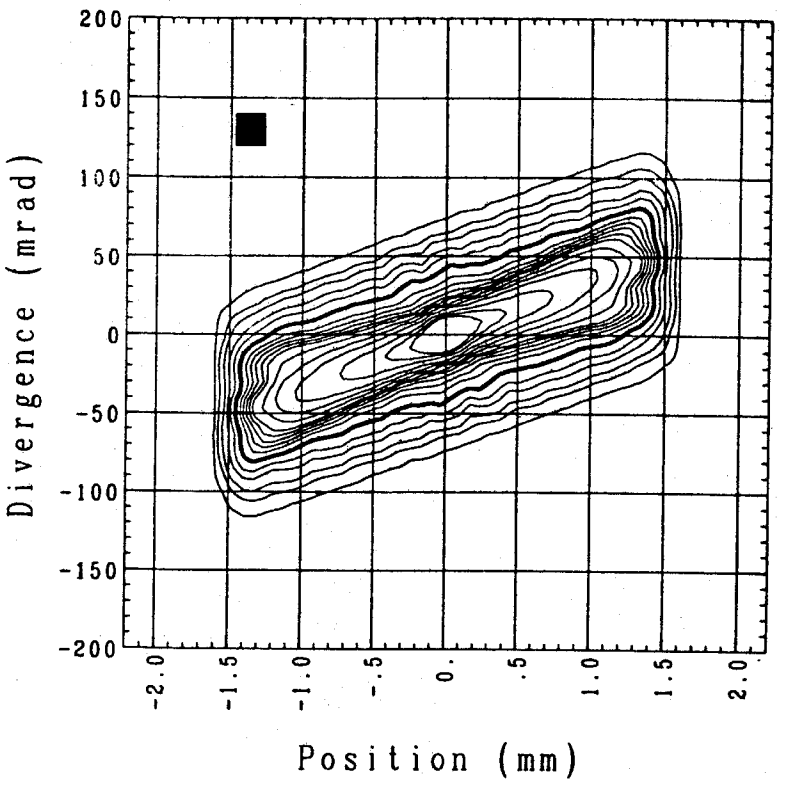

Fig. 9. Phase space contours of equal brightness for the SNICS geometry shown in fig. 6. These contours listed in table 3 correspond to a 3-mm exit aperture and a 3-kV cathode potential. The heavy-lined contour encloses 90% of the total beam current. An averaging window whose size is indicated by the shaded rectangle gives the calculation the same relative resolution as our emittance measuring device as explained in the text.

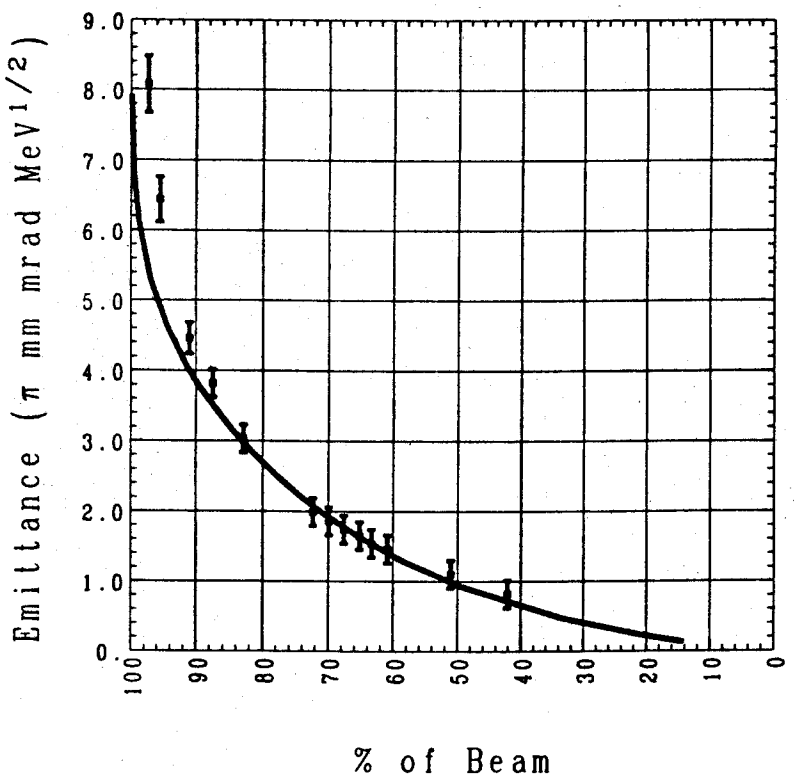

Fig. 10. Normalized emittance vs. the percent of beam enclosed by the contours shown in fig. 9. (See also table 3.) The curve is a calculation and the individual points are measurements for a Ni^- beam for the same operating conditions as the calculation.

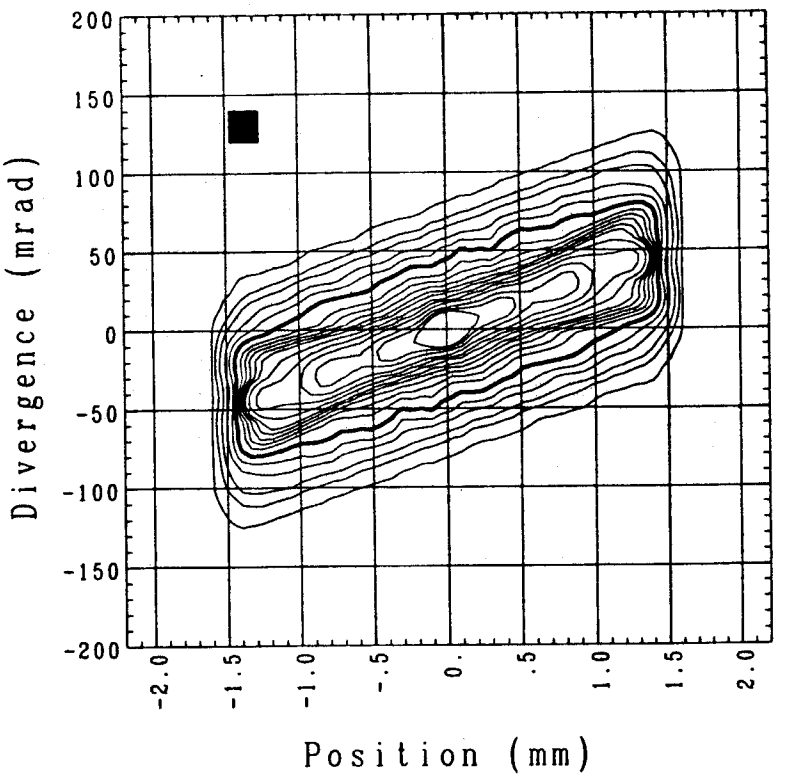

Fig. 11. Brightness contours for the same geometry as fig. 9 but for a 2-kV cathode potential. The beam spreads out more than it does for a 3-kV cathode leading to larger area in the (x,x') plane.

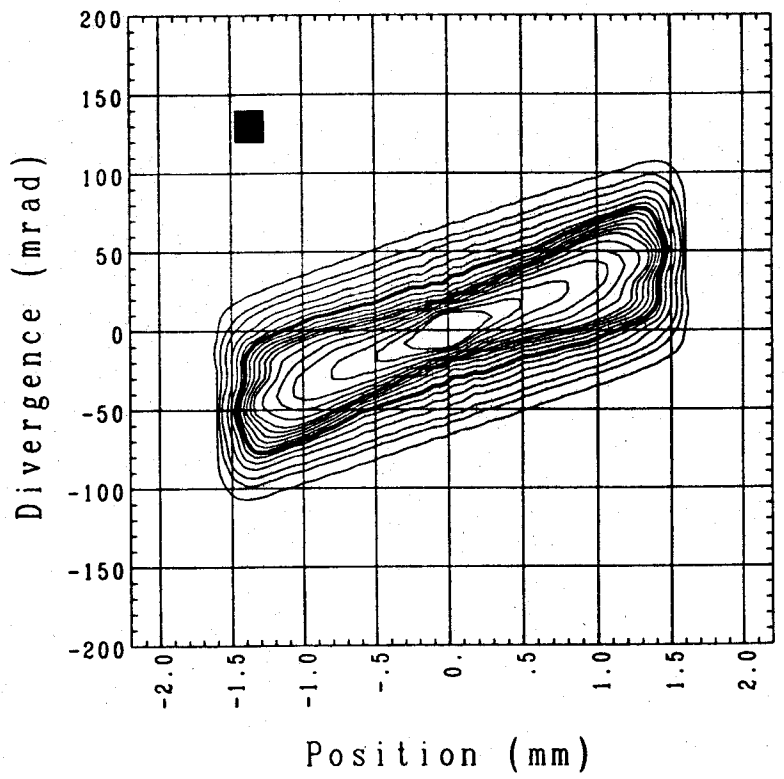

Fig. 12. Brightness contours for the same geometry as figs. 9 and 11 but for a 5-kV cathode potential. Negative ion trajectories are bunched forward by the higher cathode voltage leading to smaller area in the (x,x') plane than for a 2- or 3-kV cathode.

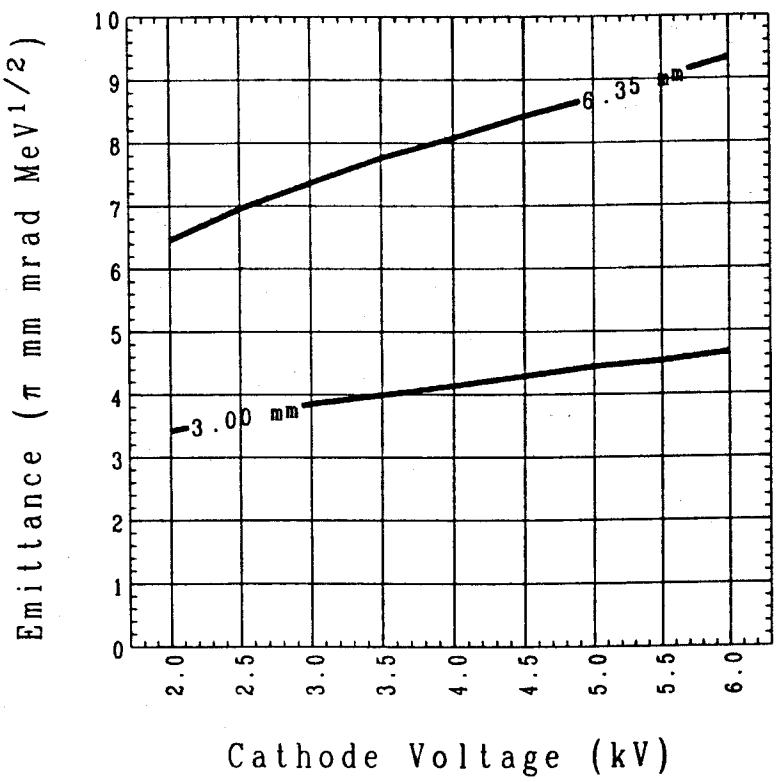

Fig. 13. Normalized emittance for 90% of the total beam current vs. sputter cathode voltage for exit aperture diameters of 3.00 mm and 6.35 mm. These curves correspond to the SNICS geometry of fig. 6.

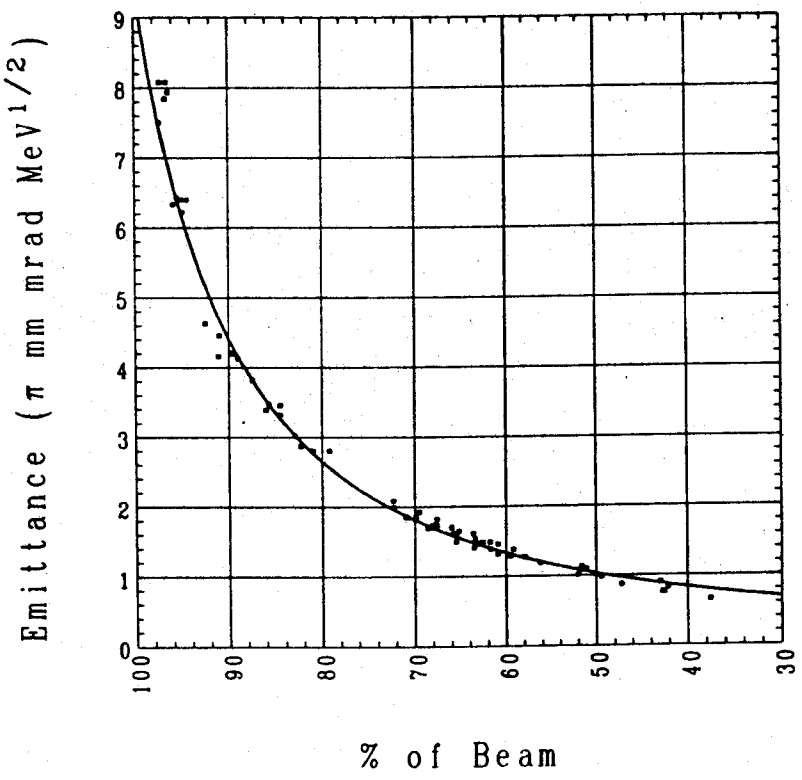

Fig. 14. Normalized emittance vs. percent of beam. Individual points are emittance measurements scaled by the factor $(3/V)^{0.309}$ where V is the cathode voltage in kV corresponding to each measurement. Data were obtained at five different cathode voltages. The curve is a plot of eq. 11 for P = 0.309 and illustrates that the experimentally obtained emittance exhibits approximately the same power law dependence as predicted by the calculations of emittance.

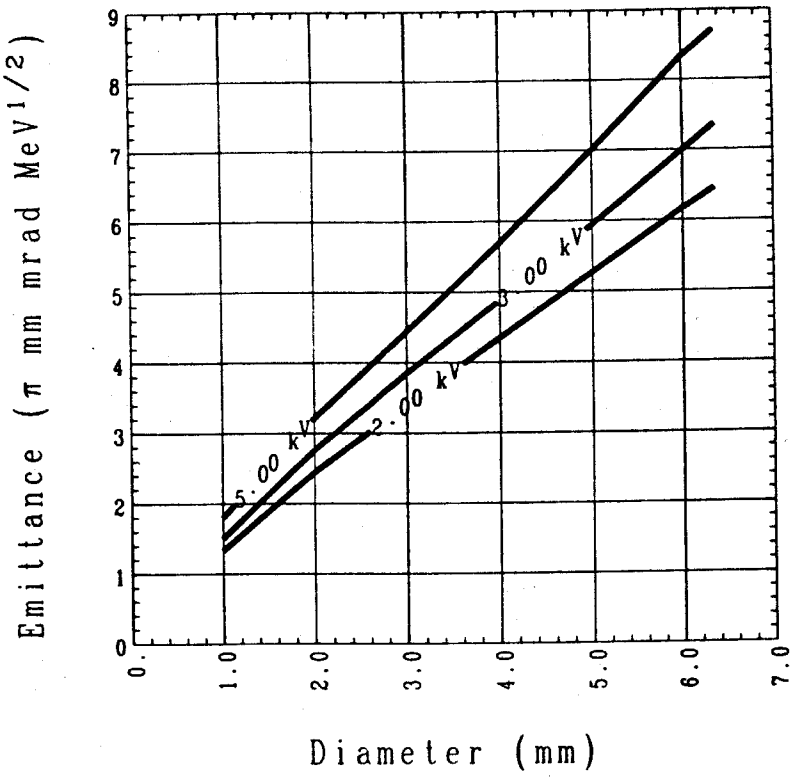

Fig. 15. Normalized emittance for 90% of the beam vs. exit aperture diameter for cathode voltages of 2, 3 and 5 kV. These curves correspond to the SNICS geometry shown in fig. 6.

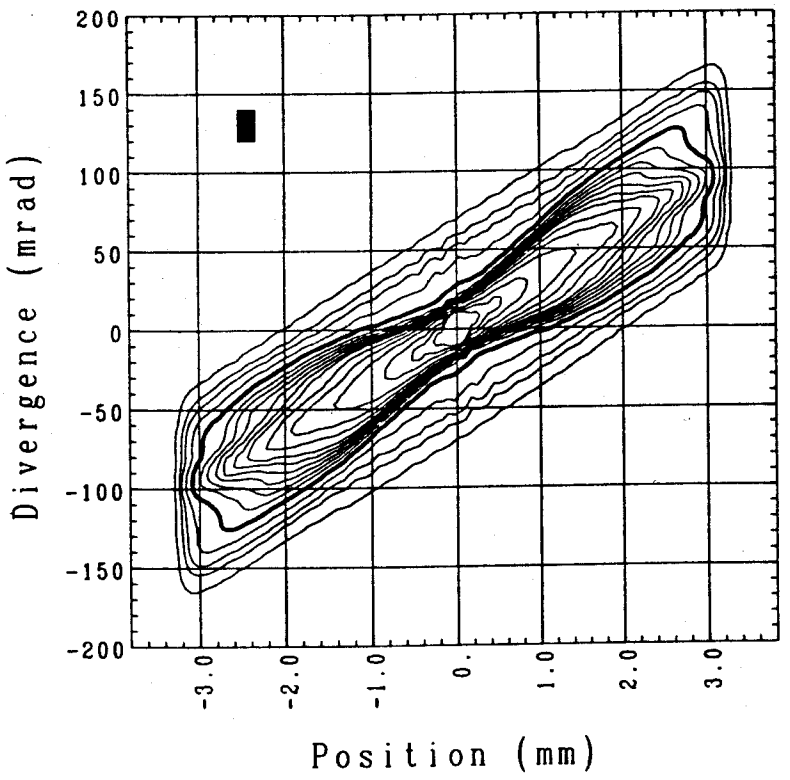

Fig. 16. Phase space contours of equal brightness for the same source geometry and 3-kV cathode voltage as fig. 9 but for a 6.35-mm diameter exit aperture.

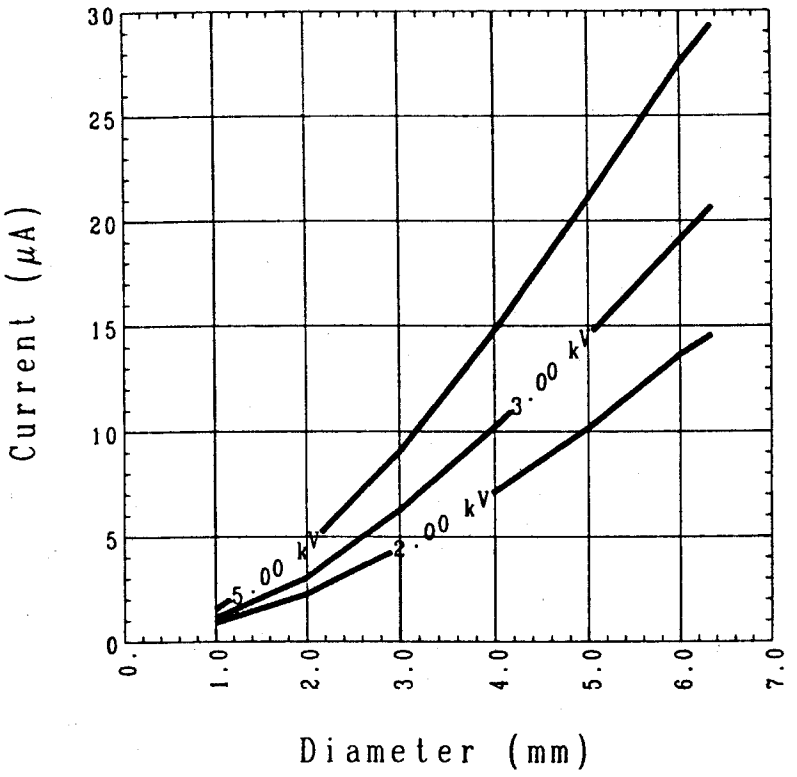

Fig. 17. Beam current vs. exit aperture diameter for cathode voltages of 2, 3 and 5 kV. These curves correspond to the SNICS geometry shown in fig. 6. They represent the 90% portion of the total beam current whose emittance is displayed in fig. 15.

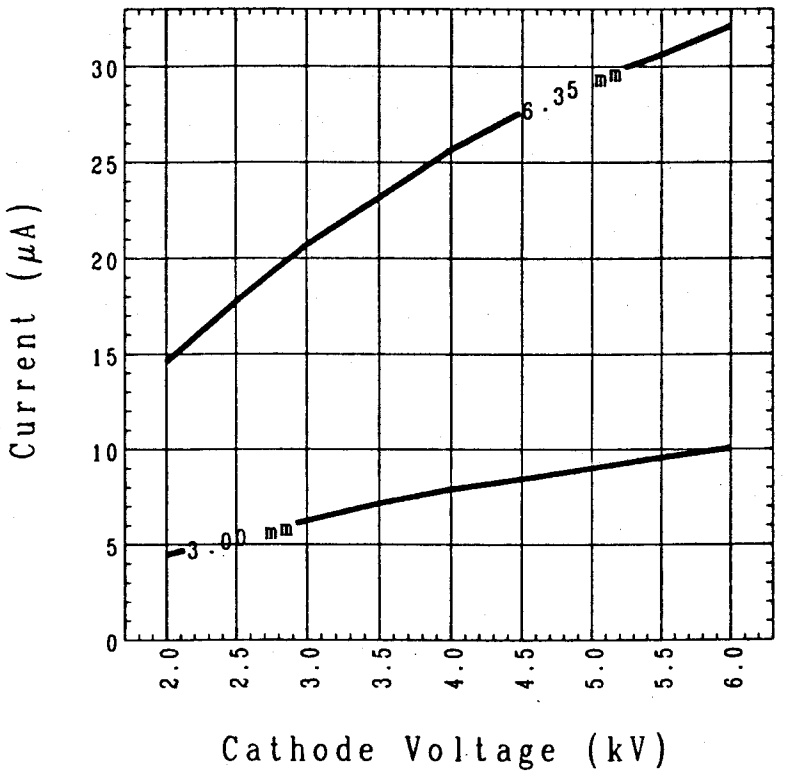

Fig. 18. Beam current vs. sputter cathode voltage for exit aperture diameters of 3.00 mm and 6.35 mm. These curves correspond to the SNICS geometry shown in fig. 6 and they represent the 90% portion of the total beam current whose emittance is displayed in fig. 13.

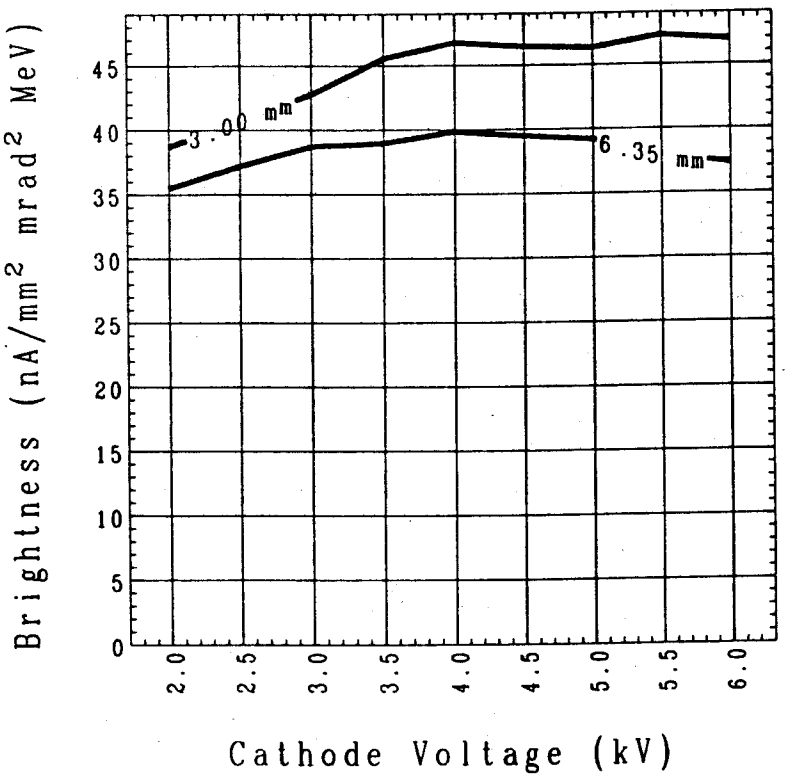

Fig. 19. Average brightness for 90% of the beam vs. sputter cathode voltage for exit aperture diameters of 3.00 and 6.35 mm. These curves correspond to the SNICS geometry of fig. 6. The brightness (defined by eq. 12) is higher for the smaller aperture diameter in spite of the large increase in beam current shown in fig. 18 for the 6.35-mm aperture.

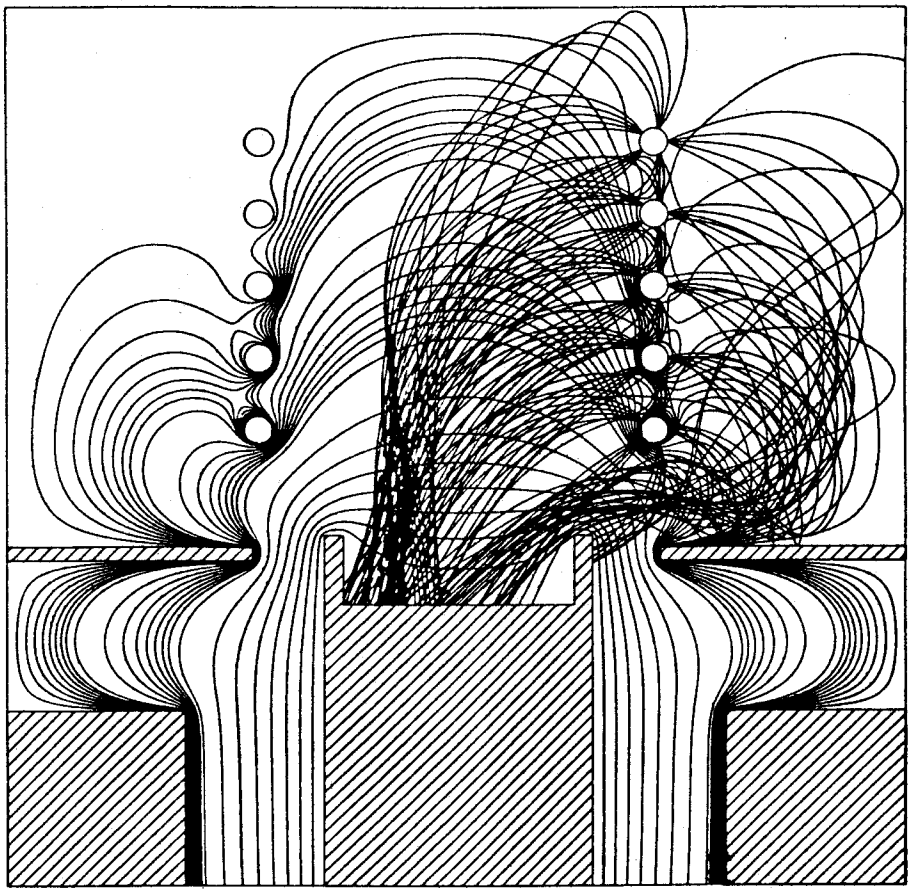

Fig. 20. Equipotentials and sample Cs^+-ion trajectories for a SNICS geometry in which the tip of the cathode forms an immersion lens. The equipotential contours correspond to the same voltages as those in figs. 4 and 6. The 2.5-mm-long sleeve protruding past the face of the cathode has little effect on the Cs^+ beam but serves to focus negative-ions sputtered from the cathode face.

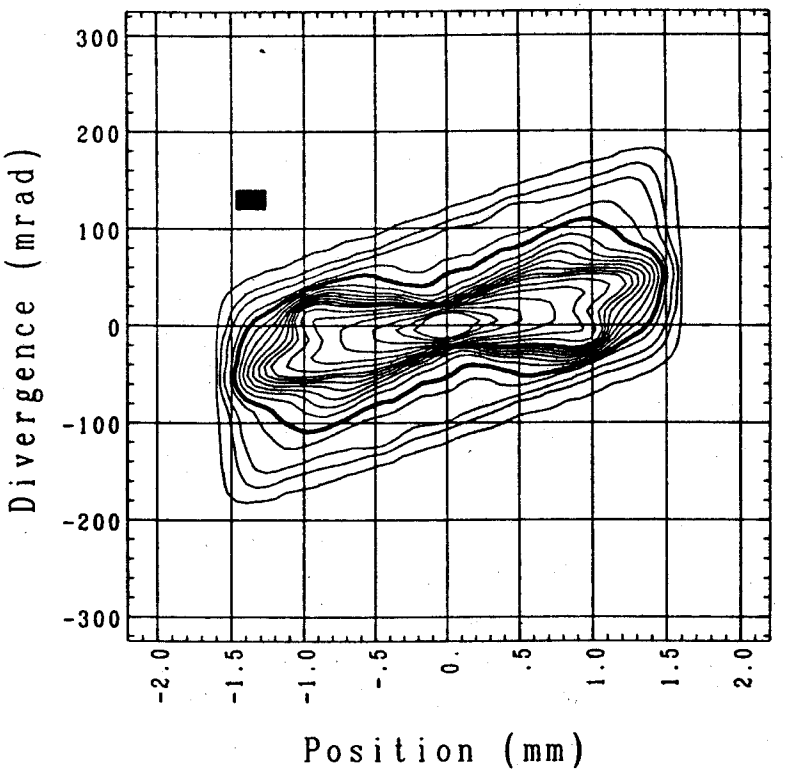

Fig. 21. Phase space contours of equal brightness for the SNICS geometry shown in fig. 20 and for a 3-mm exit aperture and a 5-kV cathode potential. The heavy lined contour encloses 90% of the total beam current. Compare to fig. 12 which corresponds to the standard SNICS geometry without an immersion lens.

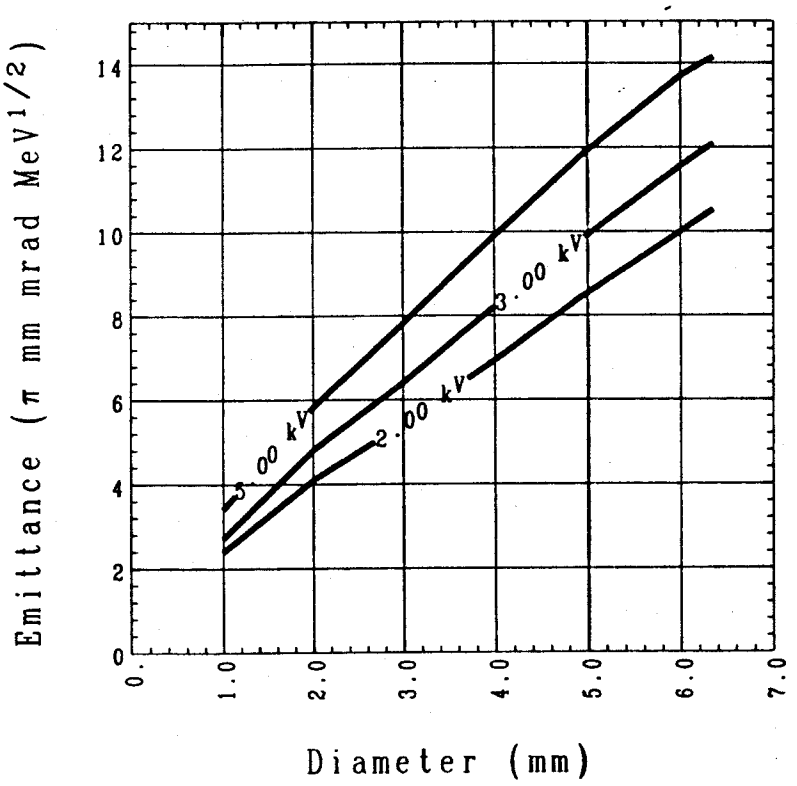

Fig. 22. Normalized emittance for 90% of the total beam current vs. exit aperture diameter for cathode voltages of 2, 3 and 5kV. These curves correspond to the SNICS geometry of fig. 20.

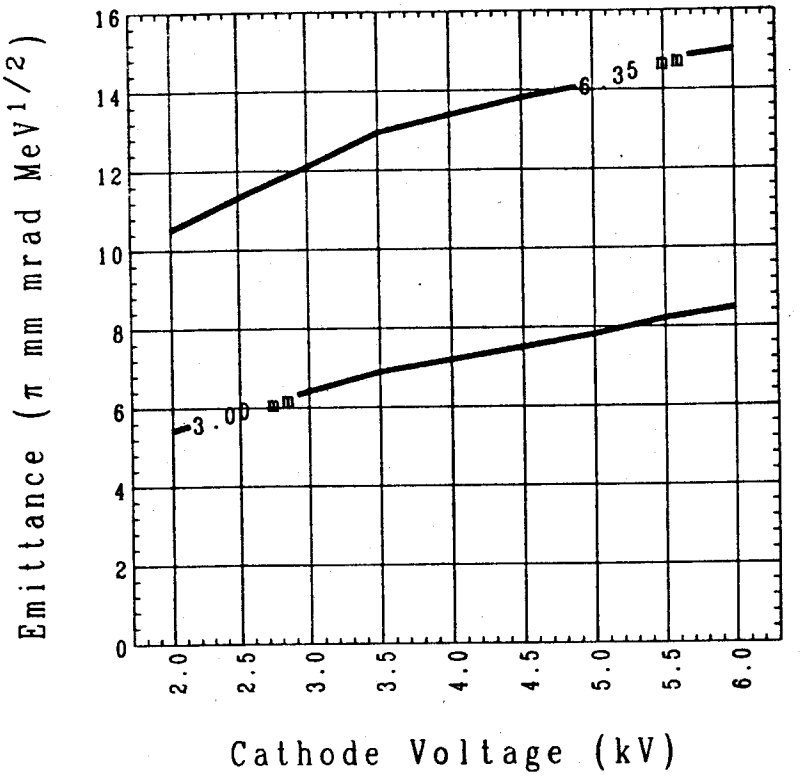

Fig. 23. Normalized emittance for 90% of the beam vs. sputter cathode voltage for exit aperture diameters of 3.00 mm and 6.35 mm. These curves correspond to the SNICS geometry of fig. 20.

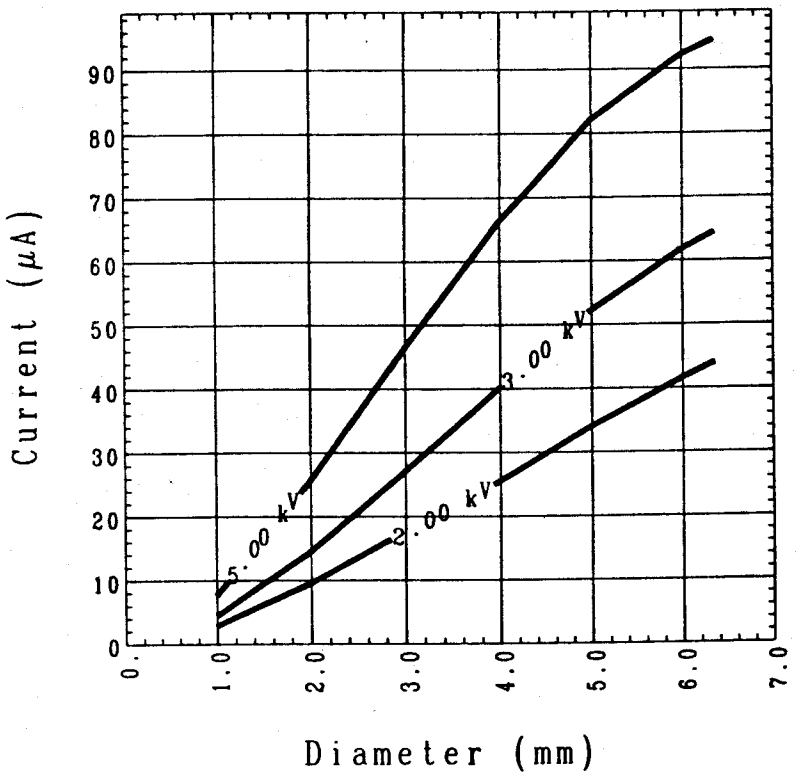

Fig. 24. Beam current vs. exit aperture diameter for the SNICS geometry of fig. 20 and for cathode voltages of 2, 3 and 5kV. These curves correspond to the 90% portion of the total beam current whose emittance is displayed in fig. 22. The 5-kV curve nearly reaches saturation since 87% of the available current is focused through a 6.35-mm aperture (see table 5).

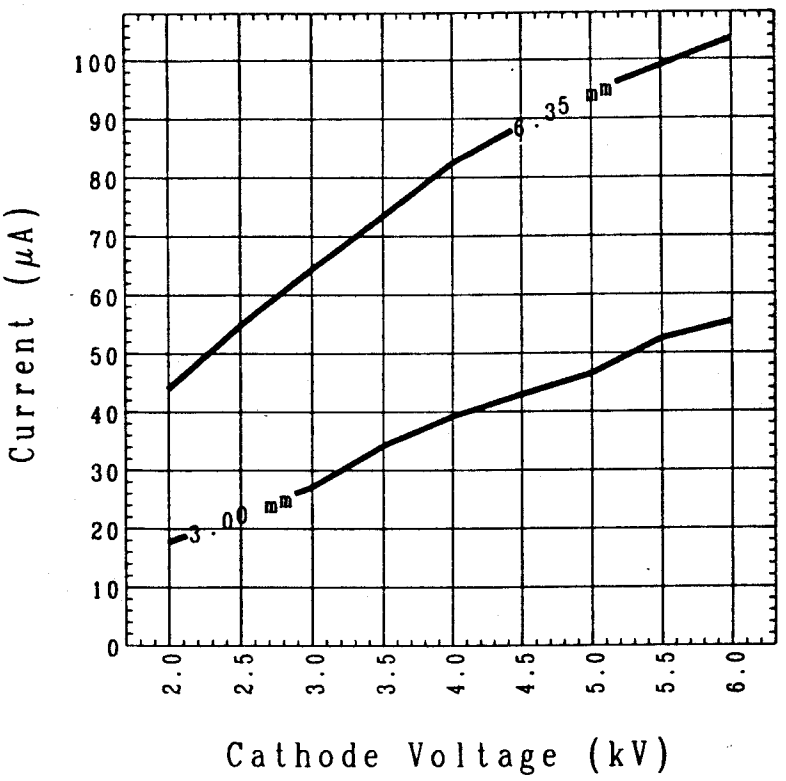

Fig. 25. Beam current vs. sputter cathode voltage for exit aperture diameters of 3.00 and 6.35 mm for the SNICS geometry of fig. 20. The 3-mm curve for this geometry in which the cathode tip is an immersion lens is entirely above the 6.35-mm curve shown in fig. 18 for the standard geometry.

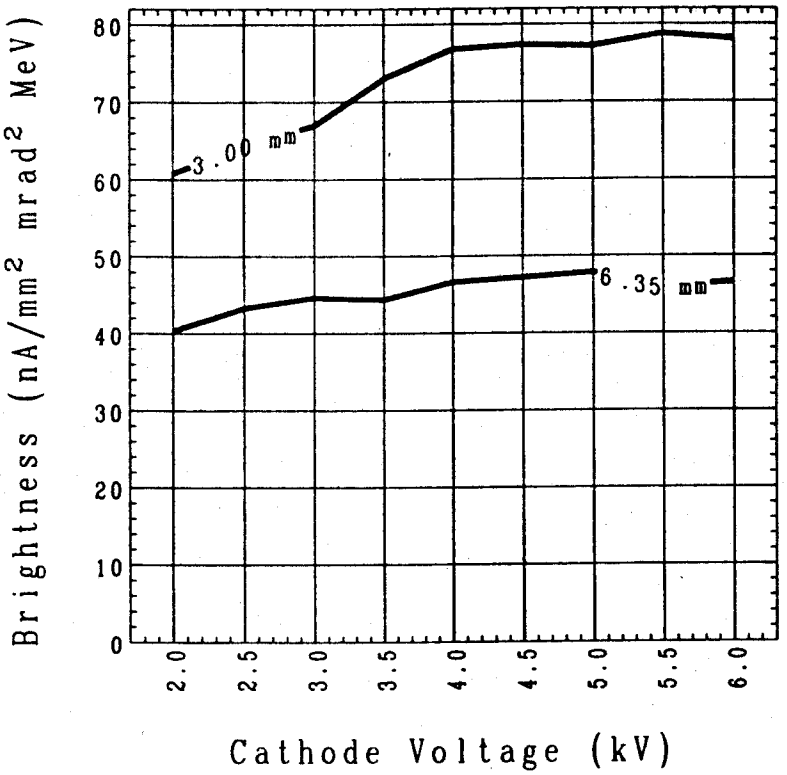

Fig. 26. Average brightness for 90% of the beam vs. sputter cathode voltage for exit aperture diameters of 3.00 and 6.35 mm. These curves correspond to the SNICS geometry of fig. 20. The addition of the immersion lens increased the average brightness for the larger aperture only slightly but the increase was by nearly 70% for the smaller aperture (see fig. 19).

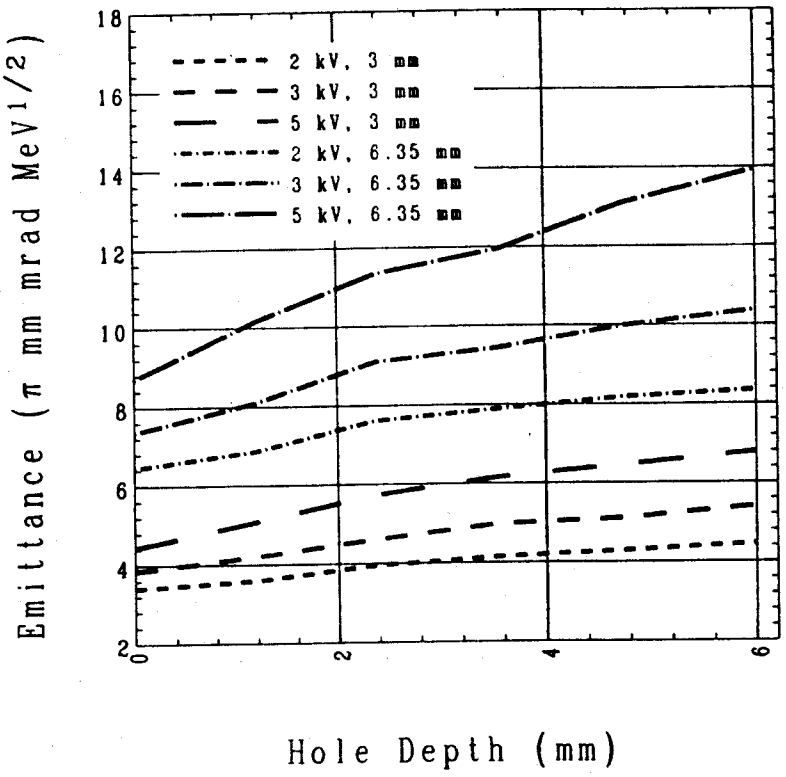

Fig. 27. Normalized emittance for 90% of the beam vs. the depth of an eroded hole in the sputter cathode for several combinations of cathode voltage and exit aperture diameter. For a hole depth of zero the source geometry is that of fig. 6.

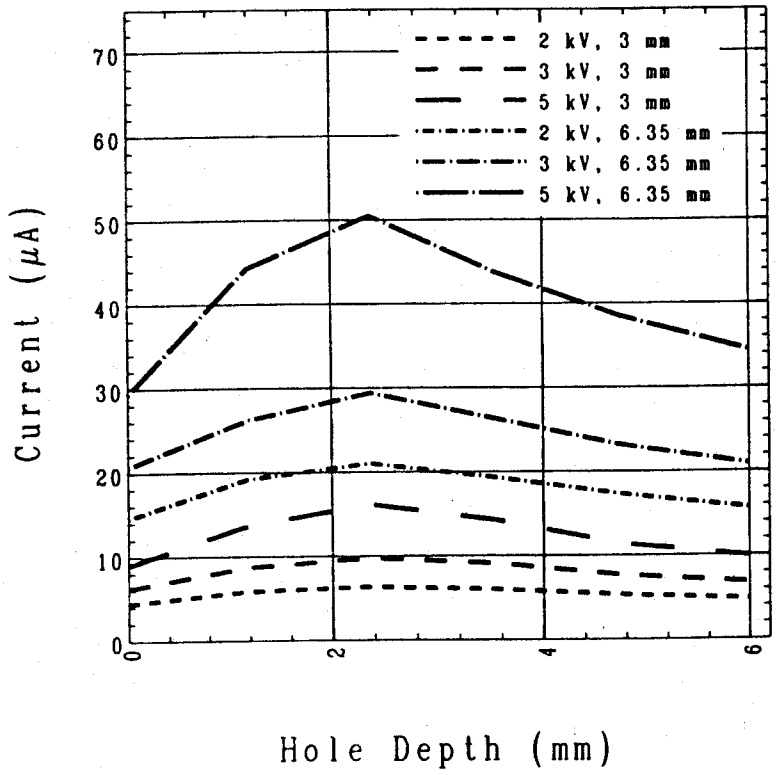

Fig. 28. Beam current vs. hole depth. These curves correspond to 90% of the total beam current whose emittance is displayed in fig. 27.

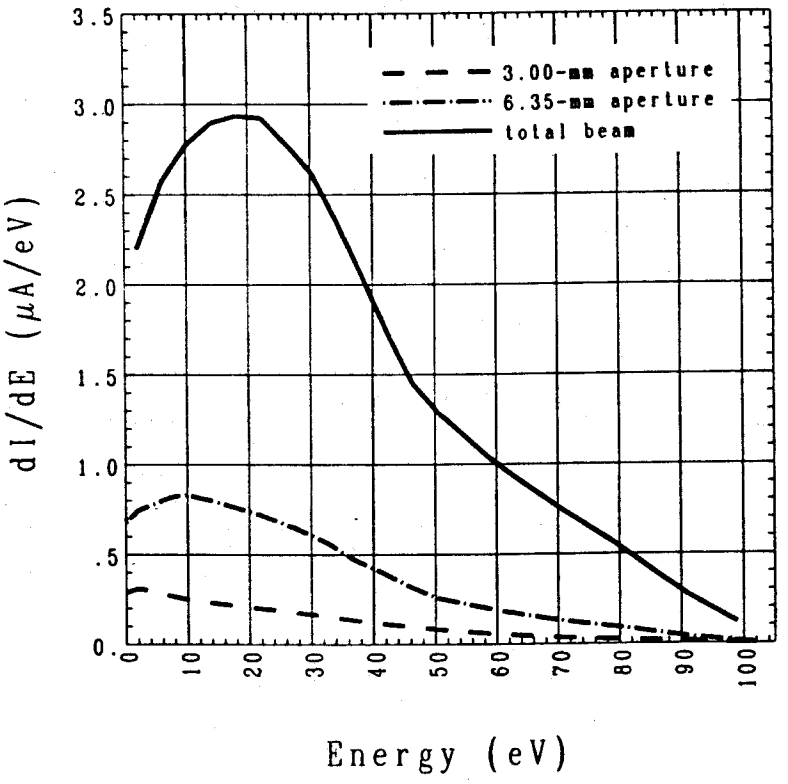

Fig. 29. Energy spectra of negative-ion beams emerging from 3.0-mm and 6.35-mm apertures for the SNICS geometry of fig. 6. For clarity the cathode voltage of 3 kV has been subtracted from ion energy plotted on the abscissa.

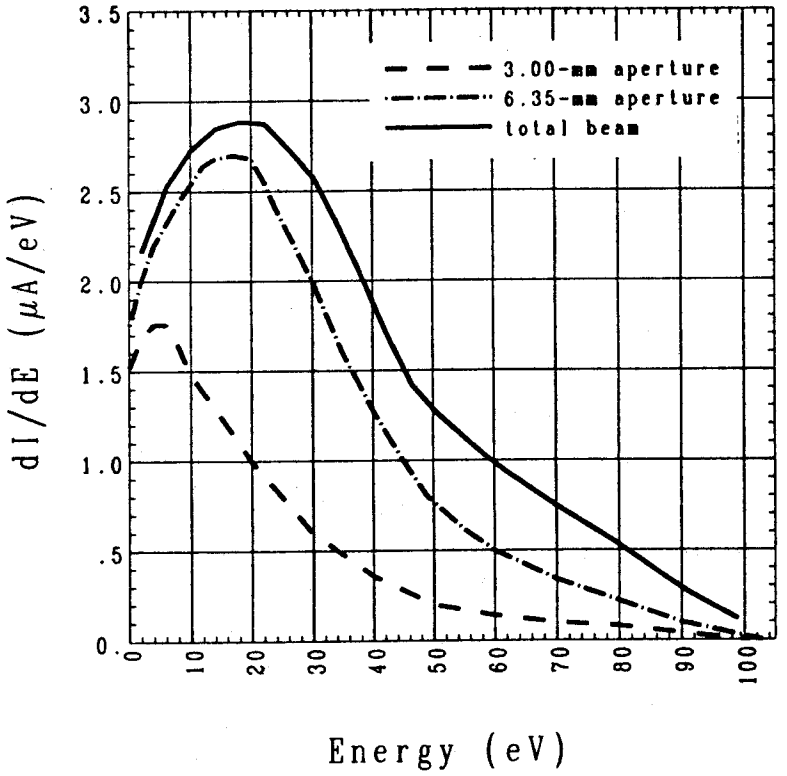

Fig. 30. Energy spectra of negative-ion beams emerging from 3.0-mm and 6.35-mm apertures for the SNICS geometry of fig. 20. These curves correspond to the same cathode voltage of 3 kV as in fig. 29.